The Backward-tracking Lagrangian Particle Method for transient viscoelastic flows

P. Wapperom, R. Keunings, V. Legat
CESAME, Division of Applied Mechanics,
Université catholique de Louvain,
B-1348 Louvain-la-Neuve, Belgium

September 8, 1999

Abstract

A new Lagrangian particle method for solving transient viscoelastic flow for both macroscopic and microscopic stress equations is proposed. In this method, referred to as the Backward-tracking Lagrangian Particle Method (BLPM), we specify the particle locations and calculate the trajectories leading to these locations. This backward tracking process is stopped after a specified time (possibly only a single time step), and the initial configuration for the Lagrangian integration of the stress is obtained by interpolating a stored Eulerian field at that time. In order to demonstrate the accuracy, efficiency and stability of the method, we consider two benchmark problems in the context of the FENE dumbbell kinetic theory of dilute polymer solutions and its FENE-P approximate constitutive equation: the high eccentricity journal bearing flow and the 4:1 contraction flow. With the help of these examples, we show in which manner accurate and stable results can be obtained, for transients of both polymer stress and stream function, with a minimum number of particles and a minimum particle path length.

Keywords: Lagrangian particle method, backward tracking, viscoelastic fluids, kinetic theory, constitutive models

1 Introduction

Until recently, numerical simulations of viscoelastic flow have been based on a purely macroscopic description. In this approach, a closed-form constitutive equation is coupled to the balance equations. Nowadays, the so-called micro-macro approach has also become feasible. In this formulation, the balance equations are complemented by a kinetic theory model to describe the rheology of the fluid. The viscoelastic contribution to the stress is obtained by a coarse-grain model of the molecular dynamics of the fluid. This avoids the need for questionable closure approximations and provides a direct link between the flow-induced development of the microstructure and the flow operating conditions. Numerical calculations with kinetic theory models can be performed using appropriate stochastic simulation techniques. The use of stochastic simulations of complex flows has been initiated in 1993 by Laso and Öttinger [1]. Recently, much progress has been made in micro-macro computations of complex problems like flow around a sphere and contraction flows. Two promising techniques are the Brownian Configuration Field method described in [2] and the Lagrangian Particle Method (LPM) developed by Halin *et al.* [3]. Briefly, LPM decouples at each time step the Eulerian finite element solution of the conservation equations and the Lagrangian computation of the polymer stress. A specified number of discrete particles is convected by the flow, and the polymer stress carried by the particles is obtained by integrating along the particle trajectories either the constitutive equation or the stochastic differential equation. By Gallez *et al.* LPM has been developed further to yield the so-called Adaptive Lagrangian Particle Method (ALPM). Here, new particles are created in regions with a low particle density and particles are annihilated in regions with a high particle density. ALPM ensures a minimum and maximum number of particles in each element. In this manner, LPM has been made suitable for highly graded meshes.

In this article, we improve LPM in a different manner. Instead of dropping the particles in the flow and following them through the flow domain, the particle positions at which the stress is evaluated are specified a priori. Next, the stress is calculated by tracking the particles backwards in time and integrating the stress equation along the obtained trajectories. We refer to the new method as the Backward-tracking Lagrangian Particle Method (BLPM).

After a short review of the governing equations in Section 2, the details of BLPM are described in Section 3. In order to validate the method and to find an optimal numerical parameter setting, BLPM is applied to the smooth high-eccentricity journal bearing flow in Section 4. We show that the number of particles per element and the tracking backwards in time can be restricted to a minimum, provided that the initial condition for the stress integral is obtained in an accurate manner. Next, in Section 5, we consider the non-smooth 4:1 contraction flow to investigate stability of the optimal method deduced from the journal bearing flow. Finally, we conclude in Section 6.

2 Governing equations

The equations governing the conservation of mass and transport of momentum are for viscoelastic incompressible flow,

$$\nabla \cdot \boldsymbol{v} = 0, \tag{1}$$

$$\rho \frac{D\boldsymbol{v}}{Dt} = -\nabla p + \nabla \cdot (2\eta_{\mathrm{s}}\boldsymbol{d} + \boldsymbol{\tau}_{\mathrm{p}}), \tag{2}$$

where ρ is the fluid density, $\boldsymbol{v}$ the fluid velocity, p the hydrodynamic pressure, and D/Dt denotes the material derivative. The extra-stress tensor has been split in a polymeric con-

tribution $\boldsymbol{\tau}_\mathrm{p}$ and a solvent contribution with η_s the solvent viscosity and $\boldsymbol{d} = (\boldsymbol{\kappa} + \boldsymbol{\kappa}^T)/2$ the rate-of-deformation tensor where $\boldsymbol{\kappa}^T$ denotes the velocity gradient.

The extra-stress tensor $\boldsymbol{\tau}_\mathrm{p}$ may either be obtained by a micro or macrorheological model. In this paper, we mainly focus on macrorheological models to validate the numerical method. For these models, we solve an equation for a non-dimensional configuration tensor $\boldsymbol{A}$ supplemented by an algebraic equation for the stress. Henceforth, we consider the so-called FENE-P model. Employing the same notation as in [3], we have

$$\frac{D\boldsymbol{A}}{Dt} = (\boldsymbol{\kappa}\cdot\boldsymbol{A} + \boldsymbol{A}\cdot\boldsymbol{\kappa}^T) + \frac{4kT}{\zeta}\boldsymbol{I} - \frac{4H/\zeta}{1-\mathrm{tr}\ \boldsymbol{A}/Q_0^2}\boldsymbol{A}, \tag{3}$$

where k is the Boltzmann constant, T the absolute temperature, ζ the friction coefficient of Brownian beads, $\boldsymbol{I}$ the unit tensor, H a spring constant, and Q_0 the maximum spring length. The polymeric stress is given by

$$\boldsymbol{\tau}_\mathrm{p} = -nkT\boldsymbol{I} + n\frac{H}{1-\mathrm{tr}\ \boldsymbol{A}/Q_0^2}\boldsymbol{A}, \tag{4}$$

where n is the dumbbell number density.

As a microscopic model, we use the FENE model which involves the end-to-end vector $\boldsymbol{Q}$ connecting two beads of a dumbbell. The distribution function ψ of the end-to-end vector is governed by a diffusion equation, see [4]. Here we use the equivalent approach where the evolution of $\boldsymbol{Q}$ is governed by a stochastic differential equation. The associated Itô stochastic differential equation (see [5]) reads,

$$d\boldsymbol{Q} = \left[\boldsymbol{\kappa}\cdot\boldsymbol{Q} - \frac{2}{\zeta}\boldsymbol{F}^c(\boldsymbol{Q})\right]dt + \sqrt{\frac{4kT}{\zeta}}d\boldsymbol{W}, \tag{5}$$

where $\boldsymbol{F}^c$ is the connector force and $\boldsymbol{W}$ the three-dimensional Wiener process, namely a Gaussian stochastic process with zero mean and covariance $\langle\boldsymbol{W}(t_1)\boldsymbol{W}(t_2)\rangle = \min(t_1,t_2)\boldsymbol{I}$. Here $\langle\cdot\rangle$ denotes the configuration space average $\int\cdot\ \psi\ \mathrm{d}\boldsymbol{Q}$. The polymeric stress can be obtained by means of the Kramers expression [4],

$$\boldsymbol{\tau}_\mathrm{p} = -nkT\boldsymbol{I} + n\langle\boldsymbol{Q}\boldsymbol{F}^c(\boldsymbol{Q})\rangle. \tag{6}$$

For the Finite Extensible Non-linear Elastic (FENE) model the connector force is given by

$$\boldsymbol{F}^c(\boldsymbol{Q}) = \frac{H\boldsymbol{Q}}{1-\boldsymbol{Q}^2/Q_0^2}. \tag{7}$$

For the FENE model no macroscopic counterpart exists. However, when the Peterlin closure approximation

$$\boldsymbol{F}^c(\boldsymbol{Q}) = \frac{H\boldsymbol{Q}}{1-\langle\boldsymbol{Q}^2\rangle/Q_0^2} \tag{8}$$

is used, the FENE-P model of Eqs. (3), (4) is obtained. The configuration tensor is then related to the end-to-end vector by $\boldsymbol{A} = \langle\boldsymbol{Q}\boldsymbol{Q}\rangle$.

The FENE and FENE-P models involve a time constant $\lambda = \zeta/4H$ and a non-dimensional finite extensibility parameter $b = HQ_0^2/kT$. We also note for further reference that the polymer contribution to the zero-shear-rate viscosity is $\eta_\mathrm{p} = nkT\lambda b/(b+3)$ for the FENE-P fluid and $\eta_\mathrm{p} = nkT\lambda b/(b+5)$ for the FENE theory.

3 Numerical method

3.1 Overall scheme

To allow for different solution methods for the balance equations and the stress equations, the numerical scheme is decoupled into two parts. The equations of motion are solved with a finite element technique, which is well-suited for a diffusion-dominated problem. The stress equation is solved by means of a method well suited for transport equations, i.e. integration along the particle trajectories. A typical time step of the overall scheme consists of the following three stages:

1. Solve the balance equations by a finite element method to obtain the velocity $\boldsymbol{v}(t_n)$ and pressure $p(t_n)$, using the Eulerian stress field $\boldsymbol{\tau}_{\mathrm{p}}^{\mathrm{E}}(t_{n-1})$;

2. Obtain the Lagrangian stress $\boldsymbol{\tau}_{\mathrm{p}}^{\mathrm{L}}(t_n)$ carried by the particles by solving the stress equations by means of a backward tracking procedure;

3. Calculate an Eulerian stress field $\boldsymbol{\tau}_{\mathrm{p}}^{\mathrm{E}}(t_n)$ from the Lagrangian stress data $\boldsymbol{\tau}_{\mathrm{p}}^{\mathrm{L}}(t_n)$ by means of a least-squares fit.

We now discuss in some more detail the various stages involved in the method.

3.2 Equations of motion

The equations of motion (1), (2) are discretised by a stabilised Galerkin approach. Choosing appropriate functional spaces for the solution and the test functions, the weak formulation becomes: Find $(\boldsymbol{v}, p, \overline{\boldsymbol{\kappa}})$ such that for all admissible weighting functions $(\boldsymbol{u}, q, \boldsymbol{f})$ we have,

$$\langle q, \nabla \cdot \boldsymbol{v} \rangle = 0, \tag{9}$$

$$\langle \boldsymbol{u}, \rho \frac{\partial \boldsymbol{v}}{\partial t} + \rho \boldsymbol{v} \cdot \nabla \boldsymbol{v} \rangle - \langle \nabla \cdot \boldsymbol{u}, p \rangle + \langle \nabla \boldsymbol{u}, 2\eta_{\mathrm{s}} \boldsymbol{d}(\boldsymbol{v}) + \boldsymbol{\tau}_{\mathrm{p}} + 2\overline{\eta}(\boldsymbol{d}(\boldsymbol{v}) - \overline{\boldsymbol{d}}) \rangle = \langle \boldsymbol{u}, \boldsymbol{t} \rangle_{\Gamma}, \tag{10}$$

$$\langle \boldsymbol{f}, \boldsymbol{\kappa}(\boldsymbol{v}) - \overline{\boldsymbol{\kappa}} \rangle = 0, \tag{11}$$

where $\langle ., . \rangle$ and $\langle ., . \rangle_{\Gamma}$ denote appropriate inner products on the domain Ω and boundary Γ, respectively, and $\boldsymbol{t}$ is the contact force. Compared to the regular Galerkin method, an extra term $2\overline{\eta}(\boldsymbol{d}(\boldsymbol{v}) - \overline{\boldsymbol{d}})$ containing an auxiliary viscosity $\overline{\eta}$ and the projected rate-of-deformation tensor $\overline{\boldsymbol{d}} = (\overline{\boldsymbol{\kappa}} + \overline{\boldsymbol{\kappa}}^T)/2$ are introduced. This so-called Discrete Elastic-Viscous Stress Splitting (DEVSS) method proposed in [6], [7] increases the stability of the scheme. It has also been used to stabilise Discontinuous Galerkin formulations for macroscopic models [7] and the Brownian Configuration Field method for microscopic models [2]. Discretisation in time has been performed by the Euler forward / Euler backward predictor-corrector scheme with a fixed time step Δt. For the discretisation in space of the the velocity we use a biquadratic continuous polynomial representation, while both pressure and projected velocity gradient are represented by a bilinear continuous polynomial. For the polymeric stress $\boldsymbol{\tau}_{\mathrm{p}}$ we use a bilinear discontinuous polynomial representation.

3.3 Stress equation

The stress equations are solved by means of a backward tracking procedure. It consists of tracking the particle motion backward in time and integrating the constitutive or stochastic equation along the obtained particle trajectories. Both stages are discussed in detail in the remainder of this section.

3.3.1 Backward tracking of particles

In BLPM the particle positions at the *current* time are specified a priori in each element of the mesh. Then, the particle trajectories leading to these locations are calculated by tracking backward in time. This allows us to keep fixed the particle positions at current time, i.e. they are not a function of time. We will denote this fixed particle position by $\boldsymbol{r}_B$. Only the particle trajectory leading to that position changes from one time step to the next, so that usually different Lagrangian particles arrive in $\boldsymbol{r}_B$ as time evolves.

A particle trajectory is described by the kinematic equation

$$\frac{\mathrm{d}\boldsymbol{r}}{\mathrm{d}t} = \boldsymbol{v}(\boldsymbol{r}, t) \tag{12}$$

For a given arbitrary particle position $\boldsymbol{r}_B$ in the flow domain at current time t_B, the particle position $\boldsymbol{r}_I$ at time $t_I < t_B$ is simply obtained by means of integration of (12) backwards in time,

$$\boldsymbol{r}_I = \boldsymbol{r}_B - \int_{t_I}^{t_B} \boldsymbol{v}\ \mathrm{d}t. \tag{13}$$

If we apply the same time step as used for the equations of motion, we have $t_B = t_n$ and $t_I = t_{n-N}$, and the time integral is divided into N intervals of length Δt. For the moment the number of intervals N remains unspecified. With the help of numerical simulations of Sections 4 and 5, we discuss a proper choice of this parameter. The time-integral in (13) is now discretised as,

$$\int_{t_I}^{t_B} \boldsymbol{v}\ \mathrm{d}t = \sum_{i=n-N+1}^{n} \int_{t_{i-1}}^{t_i} \boldsymbol{v}(\boldsymbol{r}, t_i)\ \mathrm{d}t, \tag{14}$$

which corresponds to calculating N integrals, where integral number i uses the velocity $\boldsymbol{v}(\boldsymbol{r}, t_i)$ along the trajectory between $\boldsymbol{r}(t_{i-1})$ and $\boldsymbol{r}(t_i)$. At the end point of the trajectory we have $\boldsymbol{r}(t_n) = \boldsymbol{r}_B$. Each integral over $\Delta t = t_i - t_{i-1}$ is evaluated by using a fourth-order Runge–Kutta scheme, similar to [3]. The situation is represented schematically in Fig. 1 for one particle and $N = 3$. The evaluation of the whole integral requires all intermediate velocity fields between t_{n-N} and t_n, so that N finite element velocity fields have to be stored, and the amount of work is N times that of a single time step particle tracking method. The array containing the N most recent velocity fields has to be updated every time step. Field N is annihilated, the fields $1, \ldots, N-1$ become fields $2, \ldots, N$ and the first field is filled with the most recent velocity field obtained by solving the equations of motion at the current time level. The tracking has to be performed for all particles in the flow. Thus, to keep both memory requirements and CPU time as low as possible for BLPM, both N and the number of particles should be kept as small as possible.

During the initial stages of the flow, the current time might be smaller than the total tracking time $N\Delta t$. In that case the tracking is stopped when the initial time $t = 0$ is reached. This means that the tracking only has to be performed over $\min(n, N)\Delta t$. Another special case occurs when a particle is leaving a domain boundary. Apart from numerical errors in the tracking, particles should only leave the domain at an inlet boundary for backward tracking. We denote the time at which a particle crosses the inlet by t^*. Next, for the remaining time to track back $t_{n-N} < t < t^*$, the particle is assumed to be an Eulerian particle, that is it has fixed coordinates. This procedure is similar to the handling of inlet boundaries for the forward tracking method ALPM [8]. There, Eulerian particles are fixed at the inlet and when needed a copy of it is dropped in the flow to ensure that all elements contain a sufficient number of particles.

The kinematic equation (12) is solved on the parent element [9]. Developing the derivative of $\boldsymbol{r}$ in terms of the local coordinates $\boldsymbol{\xi}$ results in the pathline equation in a parent element,

$$\frac{\mathrm{d}\boldsymbol{\xi}}{\mathrm{d}t} = \boldsymbol{J}^{-1} \cdot \boldsymbol{v}, \tag{15}$$

where $\boldsymbol{J} = \partial \boldsymbol{r}/\partial \boldsymbol{\xi}$ is the Jacobian matrix describing the mapping between the local coordinates $\boldsymbol{\xi}$ and the global coordinates $\boldsymbol{r}$. Starting from the local coordinates of the fixed particle locations, integrating Eq. (15) gives the local coordinates of the initial locations $\boldsymbol{r}_I = \boldsymbol{r}_{n-N}$.

In case a particle leaves at another boundary than the inlet, we have to proceed slightly differently. Because of the accurate tracking of the particles, we have never encountered this at non-moving walls, axes of symmetry or outlet boundaries. In our numerical simulations, we have observed that only for non-straight moving boundaries, such as present in journal bearing and free surface flows, particles at or very close to such boundaries may leave the domain due to small numerical approximation errors. To circumvent this anomalous and unphysical tracking, the velocity field is filtered to exactly satisfy the boundary conditions at the parent element. In other words, it is critical for this scheme that the boundary conditions for tracking are exactly satisfied, even if it increases slightly the residual error of the partial differential equation. In order to fulfil the boundary conditions, particles that hit such a boundary are tracked further along it. To do so, the (ξ, η)-velocity $\mathrm{d}\boldsymbol{\xi}/\mathrm{d}t$ is projected on the boundary of the reference element by

$$\frac{\mathrm{d}\boldsymbol{\xi}^*}{\mathrm{d}t} = \frac{\mathrm{d}\boldsymbol{\xi}}{\mathrm{d}t} - \boldsymbol{n}\boldsymbol{n} \cdot \frac{\mathrm{d}\boldsymbol{\xi}}{\mathrm{d}t}, \tag{16}$$

so that we just take into account the component tangential to the boundary. Due to small numerical errors, a particle on a boundary may also migrate from that boundary into the interior of the flow domain. We have chosen not to avoid this, to restrict the particle tracking as less as possible. Thus a particle encountering a boundary during integral i in Eq. (14), may return to the interior due to small numerical errors in the consecutive integrals.

3.3.2 Integration of constitutive and kinetic theory equations

For the macroscopic FENE-P model (3) an ordinary differential equation along the particle trajectories is solved for the configuration tensor. For convenience, the equations are written in non-dimensional form as in [10],

$$\frac{\mathrm{d}\boldsymbol{A}}{\mathrm{d}t} = \boldsymbol{\kappa} \cdot \boldsymbol{A} + \boldsymbol{A} \cdot \boldsymbol{\kappa}^T + \left(\boldsymbol{I} - \frac{1}{1 - \mathrm{tr}\ \boldsymbol{A}/b} \boldsymbol{A} \right), \tag{17}$$

where $\boldsymbol{A}$ and $\boldsymbol{\kappa}$ vary along the particle trajectory. Starting from an initial condition $\boldsymbol{A}_{n-N}$, the configuration tensor at $\boldsymbol{r}_B$ and at current time is obtained by integration of (17) over the N intervals of the particle trajectory, using the velocity gradients $\boldsymbol{\kappa}[\boldsymbol{r}(t_i), t_i]$ at the various time levels. Over each interval the integration is performed with a semi-implicit predictor-corrector scheme. This scheme ensures that $0 \leq \mathrm{tr}\ \boldsymbol{A} < b$. For the velocity gradients $\boldsymbol{\kappa}(t_i)$ we need an array of ancient velocities $\boldsymbol{v}(t_i)$. This was already needed for the backward tracking, thus no extra storage for the velocity gradient $\boldsymbol{\kappa}$ has to be performed. However, instead of the discontinuous velocity gradient $\boldsymbol{\kappa}$, one may also use the projection of the velocity gradient $\overline{\boldsymbol{\kappa}}$ in the right-hand side of Eq. (17). Then an extra array of projected velocity gradients has to be stored as well. We will refer to this with the label Continuous Gradients (CG). For

the initial condition, we need a configuration field at time $N\Delta t$ earlier, $\boldsymbol{A}_{n-N}$. Note that, although we just need $\boldsymbol{A}_{n-N}$ at every time step, all intermediate fields (at times between t_{n-N} and t_n) have to be stored because every new time step an $\boldsymbol{A}$ field at a time Δt later is needed. In principle, one can take N so large that the tracking backward is performed till $t = 0$. At that time, the initial value can be obtained exactly and the integration of the configuration tensor is over the whole particle trajectory. In numerical simulations, of course, the time to track back has to be kept as small as possible for reasons of efficiency.

The initialisation process for obtaining the initial value of the configuration tensor $\boldsymbol{A}_{n-N}$ is very delicate. The numerical scheme fails when the constraints tr $\boldsymbol{A} < b$ or det $\boldsymbol{A} > 0$ are violated. There are two main causes for this. The first one is in the least-squares method to obtain an Eulerian field at current time t_n from the Lagrangian values at the particle positions. The second cause is the (non-linear) polynomial interpolation or extrapolation of this Eulerian field N time steps later, to obtain the initial values of the configuration tensor at the starting points of the particle trajectories $\boldsymbol{r}_{n-N}$. In Fig. 2 the situation is illustrated with the aid of a simple one-dimensional case. A way to satisfy the constraints would be to use a least-squares method and interpolation formulas that respect these constraints. For reasons explained below, we have proceeded differently.

To ensure tr $\boldsymbol{A} < b$ during the initialisation process we proceed as follows. First we transform the obtained configuration tensor at time t_n at the particle positions in a tensor $\boldsymbol{F}$,

$$\boldsymbol{F} = \frac{\boldsymbol{A}}{1 - \text{tr } \boldsymbol{A}/b} \tag{18}$$

for which the relation $0 <$ tr $\boldsymbol{F} < \infty$ holds. From the values of $\boldsymbol{F}$ at the particle positions, an Eulerian field $\boldsymbol{F}^{\text{E}}$ is computed with the help of a least-squares method. Similar to the stress field, we will use discontinuous polynomials to represent $\boldsymbol{F}^{\text{E}}$. A suitable polynomial order will be explored with the aid of numerical simulations in Sec. 4. N time steps later, the field $\boldsymbol{F}^{E}$ is used for initialisation of the Lagrangian tensor $\boldsymbol{F}^{\text{L}}_{n-N}$ at the initial positions of the particle trajectories $\boldsymbol{r}_{n-N}$. At these particle positions, we finally transform the tensor field back to the configuration tensor to obtain the initial value of $\boldsymbol{A}$ for the integration along the particle trajectories. By taking the trace of Eq. (18) and performing some algebraic operations, it is easily verified that the inverse transformation is given by

$$\boldsymbol{A} = \frac{\boldsymbol{F}}{1 + \text{tr } \boldsymbol{F}/b}. \tag{19}$$

By taking the trace of this equation and rewriting its right-hand side as b tr $\boldsymbol{F}/(b +$ tr $\boldsymbol{F})$, immediately shows that the condition tr $\boldsymbol{A} < b$ is indeed fulfilled. Performing the least-square method and interpolation on $\boldsymbol{F}$ instead of $\boldsymbol{A}$ is not only useful to fulfil the constraint tr $\boldsymbol{A} < b$ but also to circumvent large approximation errors. Close to b, small numerical approximation errors in $\boldsymbol{A}$ may lead to large errors in the stress, because of the factor $1/(1 -$ tr $\boldsymbol{A}/b)$.

To ensure that det $\boldsymbol{A} > 0$, a transformation as described above for the trace is not obvious. As this is only a problem for the FENE-P model, and not for the FENE model, we have chosen a relatively simple correction method. The method ensures that the constraint is fulfilled, but it locally decreases the accuracy of the interpolation. Before we transform $\boldsymbol{F}^{\text{L}}$ back into $\boldsymbol{A}^{\text{L}}$ at the the initial particle positions $\boldsymbol{r}_{n-N}$, we correct $\boldsymbol{F}^{\text{L}}$ to a tensor with a small positive determinant ϵ (note that a positive det $\boldsymbol{A}$ implies a positive det $\boldsymbol{F}$ and vice versa). We correct on $\boldsymbol{F}$ because this ensures that we still fulfil the constraint tr $\boldsymbol{A} < b$ and

it avoids large errors in the stress, as explained above. To obtain a positive determinant, we first correct all negative diagonal elements F_{ii} to small positive values ϵ. Then, in case $F_{11}F_{22} - F_{12}^2$ is negative a 2D isotropic term is added so that $F_{11}F_{22} - F_{12}^2 = \epsilon$. The small parameter is taken as $\epsilon = 10^{-9}$. From our numerical simulations we have observed that this correction is only needed in a limited number of positions in the flow domain, e.g. near discontinuities or steep gradients, and that it is necessary to avoid divergence of the integration along the particle trajectories. For example, for the fine mesh used for the 4:1 contraction flow we had to correct the determinant at six particle locations close to the sharp corner. Finally, we remark that a negative determinant of $\boldsymbol{A}$ could also occur during the integration along a trajectory, but we did not observe this in our numerical simulations.

To obtain the stress for the FENE kinetic-theory model (5) we solve a stochastic equation for the end-to-end vector $\boldsymbol{Q}$ along the particle trajectories. Each particle contains N_d dumbbells with end-to-end vectors $\boldsymbol{Q}_j$, $j = 1, \cdots, N_d$. For each individual realisation $\boldsymbol{Q}_j$ the non-dimensional equation [10] reads,

$$d\boldsymbol{Q}_j = \left[\boldsymbol{\kappa} \cdot \boldsymbol{Q}_j - \frac{1}{2}\boldsymbol{F}^c(\boldsymbol{Q}_j)\right] dt + d\boldsymbol{W}_j, \tag{20}$$

where $\boldsymbol{Q}_j$ and $\boldsymbol{\kappa}$ vary along the particle trajectory. We adopt the method of variance reduction, as described in [2] for the Brownian Configuration Field method. This implies that the same Wiener process is taken in each j-th dumbbell of each particle. A meaningful interpolation can thus be performed in the initialisation process. Furthermore, apart from decreasing the cost of generating the random numbers, variance reduction also dramatically reduces the spatial fluctuations of the velocity and stress fields, as pointed out in [2], [11].

Starting from the previously computed $\boldsymbol{Q}_j(t_{n-N})$ as initial condition for realisation j, the end-to-end vector $\boldsymbol{Q}_j(t_n)$ at the fixed particle position $\boldsymbol{r}_B$ is obtained by integration along the particle trajectory. Over each of the N intervals of the trajectory the integration is performed with a semi-implicit predictor-corrector scheme proposed in [5]. This scheme is of weak order two and ensures that $0 \leq \boldsymbol{Q}_j^2 < b$. The velocity gradients $\boldsymbol{\kappa}$ are handled similarly as for the FENE-P model. For the initial condition, however, we now need to store Eulerian fields for all realisations $\boldsymbol{Q}_j$. For each $\boldsymbol{Q}_j$ we take a discontinuous polynomial representation, as for the polymer stress $\boldsymbol{\tau}_\mathrm{p}$. A suitable polynomial order will be discussed on the basis of numerical simulations. Also note that, although we just need $\boldsymbol{Q}_j(t_{n-N})$ at every time step, all intermediate fields (at times between t_{n-N} and t_n) have to be stored because every new time step a $\boldsymbol{Q}_j$ field at a time Δt later is needed. And, as we need all realisations $\boldsymbol{Q}_j$, this severely restricts the number of backward-tracking steps N in the numerical simulations. For the FENE kinetic theory model the initialisation process is less complicated than for the FENE-P model, because it is represented by a vector $\boldsymbol{Q}_j$ instead of a tensor $\boldsymbol{A}$. Furthermore, the dyadic product $\boldsymbol{Q}_j\boldsymbol{Q}_j$ is positive by definition. For the constraint $\boldsymbol{Q}_j^2 < b$ we apply a transformation as close as possible to the FENE-P equivalent (18),

$$\boldsymbol{F}_j = \frac{\sqrt{\boldsymbol{Q}_j^2}}{1 - \boldsymbol{Q}_j^2/b}\boldsymbol{Q}_j \tag{21}$$

to map $\boldsymbol{Q}_j$ to a vector $\boldsymbol{F}_j$ for which the length is not bounded.

The polymeric stress (6) carried by a particle is finally obtained by taking the ensemble average of all realisations $\boldsymbol{Q}_j$,

$$\boldsymbol{\tau}_\mathrm{p} = -\boldsymbol{I} + \frac{1}{N_d}\sum_{j=1}^{N_d} \boldsymbol{Q}_j \boldsymbol{F}^c(\boldsymbol{Q}_j), \tag{22}$$

where $\boldsymbol{\tau}_\mathrm{p} = \boldsymbol{\tau}_\mathrm{p}(\boldsymbol{r}_B)$, $\boldsymbol{Q}_j = \boldsymbol{Q}_j(\boldsymbol{r}_B)$, and N_d the number of dumbbells per particle.

What still remains is the choice in a reference element of the particle positions at which we want to calculate the Lagrangian quantity $\boldsymbol{A}$ or $\boldsymbol{Q}$. It is not a priori clear how to distribute the particles over the element. To minimise extrapolation, which may easily violate the constraint on the determinant as discussed above, some particles have to be put on the boundary and preferably at the corners of an element. Furthermore, information has to be transported from one element to the other which requires that a number particle trajectories leave the element. This can easily be understood by considering a moving front in a pure advection problem. If the trajectories do not leave an element, the solution will always remain equal to the initial state in case of a discontinuous representation of the transported variable. For short trajectories this also requires particles very close or at the boundaries. For these reasons, particles equally distributed over the interior or at the integration points will not be good options. Keeping the above considerations in mind, we discuss two alternatives, as depicted in Fig. 3 for the case of quadratic representations:

1. Particles at the nodal points. Additionally, this avoids problems with negative determinants in the least-squares method, because we have the identity mapping, and it guarantees a minimal number of particles per element (ppe);

2. An alternative particle distribution with 13 ppe having no particles at the corners.

As the nodal point distribution contains less particles, it is preferable, particularly for kinetic theory models. The second distribution is mainly included to check for possible numerical problems when particles are located exactly at discontinuities. For example, this is the case in a contraction flow for the first distribution, for which we have particles exactly at the sharp corner.

To conclude this section, we discuss the advantages and possible drawbacks of BLPM. Because the particle locations where we want to calculate the configuration quantity is specified a priori in the reference element, the distribution of the particles is controlled completely. This means that we can choose particle locations that are well distributed over each element and the number of particles can be kept as low as possible, even for highly graded meshes. Furthermore, we also eliminate a priori temporal numerical fluctuations in the stress observed in ALPM due to changes in particle distributions per element. On the other hand, the backward tracking method introduces the question of the initial condition for the integral along a trajectory. In BLPM we track backward in time and integrate N steps every time step. However, it is not clear beforehand what value of N has to be chosen to obtain accurate results. For BLPM to be an effective method, the number of backward steps N has to be kept as small as possible. This is particularly true for the microscopic models for which the integration is CPU-time consuming and much memory is needed to store the $\boldsymbol{Q}$ fields. In the remainder, we show that in combination with an accurate initialisation of $\boldsymbol{Q}$ or $\boldsymbol{A}$, tracking backward with only a single step ($N = 1$) is sufficient to obtain accurate transient results. This makes BLPM an efficient method indeed.

4 High-eccentricity journal bearing flow

4.1 Problem description

In this section we consider the transient, planar flow between eccentric cylinders. The inner cylinder of radius R_i rotates at a constant angular velocity ω, while the outer cylinder of radius R_o is kept at rest. The axes of the two cylinders are separated by an eccentricity

e. The particular flow parameters used are $R_i = 1$, $R_o = 2.5$, $e = 1$, and $\omega = 0.5$. For the fluid parameters, we select $\rho = 1$, $\eta_{\rm s} = 0.1$, $\eta_{\rm p} = 0.8$, $\lambda = 3$, and $b = 50$. Here, both flow and fluid parameters are expressed in an arbitrary consistent system of units. The geometry is characterised by the non-dimensional eccentricity $\epsilon = e/(R_o - R_i) = 0.67$ and the non-dimensional gap thickness $\mu = (R_o - R_i)/R_i = 1.5$. The fluid flow is specified by the Reynolds number $Re = \rho\omega R_i(R_o - R_i)/(\eta_{\rm s} + \eta_{\rm p}) = 0.8$, the Deborah number $De = \lambda\omega R_i/(R_o - R_i) = 1$, the non-dimensional finite extensibility parameter $b = 50$, and the viscosity ratio $\beta = \eta_{\rm s}/(\eta_{\rm s} + \eta_{\rm p}) = 1/9$. Initially, the fluid is assumed at rest, that is we specify a vanishing velocity and polymer stress. For the FENE fluid, a vanishing polymer stress is approximated by solving the equation for the end-to-end vector (20) with $\boldsymbol{\kappa} = \mathbf{0}$ and taking the obtained $\boldsymbol{Q}_j$ as the initial distribution of dumbbells. For the DEVSS method, we take the auxiliary viscosity equal to the polymeric viscosity, $\overline{\eta} = \eta_{\rm p}$.

Three meshes have been used. The coarse mesh consists of 10x40 quadrilateral elements. The medium and fine meshes are obtained by a refinement of the coarse mesh with a factor two and three in both directions, so consisting of 20x80 and 30x120 elements, respectively. The coarse mesh is depicted in Fig. 4, in which we also indicate the location where we examine the transients of stress.

4.2 Results

To establish an optimal parameter setting for BLPM, various possibilities for the number of backward steps N and the order of the field $\boldsymbol{F}^{\rm E}$ for initialisation have been investigated for the macroscopic FENE-P equation. We have used $N = 1$, 40 and 100, which corresponds to a backward tracking time of 1/60 λ, 2/3 λ and 5/3 λ, respectively. Results for the transients of normal stress N_1 and shear stress τ_{xy} are displayed in Fig. 5, obtained with the coarse mesh and a discontinuous linear field $\boldsymbol{F}^{\rm E}$. Clearly, the value of the parameter N has a big impact on the results obtained on the coarse mesh with a linear initialisation field. Results for the same values of N and the same mesh, but now using a discontinuous quadratic field $\boldsymbol{F}^{\rm E}$, are provided in Fig. 6. Here, the situation has improved dramatically. For $N = 40$ and $N = 100$, the stress transients almost coincide and the difference with the transient of $N = 1$ is small as well. This difference can be attributed to the coarseness of the mesh, and is not inherent to BLPM with $N = 1$ as shown in Fig. 7. There we have repeated the latter calculations on the medium mesh and an excellent agreement is observed over the whole transient obtained by BLPM with $N = 1$ and $N = 100$. We remark in passing that, although not shown in the figures, the nodal distribution with nine particles per element and the alternative with thirteen particles per element, do not exhibit any noticeable difference in these cases.

To verify that BLPM converges with mesh refinement we have used the three different meshes with $N = 1$ and a time step of $\Delta t = 10^{-2}$ (Fig. 8). We observe a good convergence indeed. The curves for the medium and fine meshes practically superimpose, so that the medium mesh is sufficiently refined for the current computations. Compared with the coarse mesh, only some minor differences are present in the transient stress curves.

To ensure that accuracy is also maintained for small time steps, we have used $N = 1$ with two smaller time steps Δt of 10^{-3} and 10^{-4}. The backward tracking time for the latter Δt corresponds to only 1/6000 λ. The results for the coarse mesh in Fig. 9 show an excellent agreement; in particular the transients for $\Delta t = 10^{-3}$ and $\Delta t = 10^{-4}$ do coincide. The small discrepancy with the solution using $\Delta t = 10^{-2}$ near the steady state, can again be attributed to the coarseness of the mesh. This is confirmed by Fig. 10, where the stress transients for

$\Delta t = 10^{-2}$ and $\Delta t = 10^{-4}$ are displayed on the medium mesh. Furthermore, this figure shows that the DEVSS method with $\overline{\eta} = \eta_{\rm p}$ does not noticeably decrease the accuracy of the transients in this flow geometry.

In Fig. 11, BLPM is compared to two other methods. The first one is the standard Lagrangian particle method (LPM) [3] using an average number of 1600 particles per element. The second method is a mixed Galerkin finite element approach described in [12]. The agreement on the coarse mesh is good, except maybe near the steady state where all methods slightly differ. Refining the mesh diminishes these differences drastically, as demonstrated in Fig. 12. There the results for LPM with 1600 particles and BLPM can hardly be distinguished.

Finally, we demonstrate the ability of BLPM to handle kinetic theory models. Results have been obtained for the FENE dumbbell model, using the coarse mesh of Fig. 8. In Fig. 13, BLPM is compared with the Adaptive Lagrangian Particle Method (ALPM) described in [8]. In ALPM, initially each element contains 16 particles, each containing 5000 dumbbells. During the flow, particles are created and destroyed such that a minimum number of 9 and a maximum of 20 particles per element is guaranteed. For BLPM, to compensate for the smaller amount of particles per element (i.e. nine), we have employed slightly more dumbbells per particle, namely $N_d = 6000$. Agreement is good for the entire transients. The temporal fluctuations in the steady-state solution seem however somewhat smaller for BLPM. Also given in Fig. 13 is the FENE-P solution for comparison purposes. Except for the initial stages, the FENE-P solution lies well above the FENE result, revealing the impact of the closure approximation.

5 4:1 contraction flow

5.1 Problem description

In this section, we consider the transient, planar flow in a 4:1 abrupt contraction. The inlet and outlet sections are taken equal to 20 and 40 times the downstream channel half-width L, respectively. The no-slip boundary condition is assumed to hold at the wall, and a quadratic velocity profile is prescribed at the inlet and outlet. Although a quadratic profile does not exactly match a fully developed flow, it is found that the flow is only slightly perturbed close to the inlet and outlet. Initially, a vanishing velocity and polymeric stress are specified for the whole domain. For the FENE model, a vanishing stress is simulated by solving the equation for the end-to-end vector (20) with $\boldsymbol{\kappa} = \mathbf{0}$. The obtained $\boldsymbol{Q}_j$ are then taken as the initial distribution of dumbbells. For the DEVSS method, we again take $\overline{\eta} = \eta_{\rm p}$. In this flow geometry, the DEVSS stabilisation is found indispensable at high Deborah numbers. Finally, we have used quadratic initialisation fields $\boldsymbol{F}^{\rm E}$, and one backward step ($N = 1$).

For the fluid parameters we select $\rho = 0.098$, $\eta_{\rm s} = 0.05$, $\eta_{\rm p} = 0.65$, $\lambda = 0.6$, and $b = 10$ (expressed in an arbitrary consistent system of units). The fluid flow is specified by the Reynolds number $Re = \rho V L/(\eta_{\rm s} + \eta_{\rm p}) = 1.07$, the Deborah number $De = \lambda V/L = 4.6$, the non-dimensional finite extensibility parameter $b = 10$, and the viscosity ratio $\beta = \eta_{\rm s}/(\eta_{\rm s} + \eta_{\rm p}) = 1/14$. For the characteristic velocity V we take the average velocity at the outlet.

We have used two meshes of quadrilateral elements. The coarser mesh consists of 465 elements. The finer mesh is a refinement of this mesh with a factor two in both directions, so consisting of 1860 elements. A zoom of the coarse mesh near the sharp corner is depicted in Fig. 14, where we also indicate the location where we examine the transients of stress.

5.2 Results

For the FENE-P model, the development in time of the streamlines are displayed in Fig. 15. Here we have used the DEVSS/CG method which turns out to be slightly more accurate, because less corrections for the determinant are necessary near the sharp corner than for DEVSS alone. Initially, a corner vortex develops and increases in intensity. At about $t = 0.25$, a lip vortex starts to grow at the re-entrant corner while the corner vortex diminishes. At $t = 0.85$, the two recirculation zones attach, still displaying two vortices. At later times, these two vortices merge to form one big lip vortex, whose intensity continues to increase. The steady-state solution is reached between $t = 3$ and $t = 4$ displaying one large lip vortex.

Figure 16 displays the contour lines of the the steady-state values of the stress components τ_{xx}, τ_{xy} and τ_{yy}. The contours are very smooth indeed, except near the re-entrant corner where steep gradients exist for all three components. To investigate the dependence on mesh and distribution of particles, transients of the stress at the corner are plotted in Fig. 17. It is remarkable that even at the corner point the transients of the stress are smooth. After about $t = 2$, an oscillation-free steady state is reached for all three curves. However, the numerical values of the transients and resulting steady states near the sharp corner depend quite strongly on the particle position and the refinement of the mesh, as expected. Despite these large differences in the stress, the streamline patterns remain the same as those shown in Fig. 15.

Calculations for the FENE dumbbell model have been performed on the coarse mesh. The number of dumbbells per particle is $N_d = 4800$. Results for the transient stresses are provided in Fig. 18. The shear stress is very smooth while the normal stress displays some small-amplitude oscillations typical of stochastic simulations. Comparison of Figs. 17 and 18 shows a significant qualitative difference between FENE and FENE-P results. Further mesh refinement as well as increased number of dumbbells per particle is needed to establish this observation. Field contour plots of the stress at time $t = 10$ are provided in Fig. 19. Except near the sharp corner, where steep gradients are present in all three stress components, the contour plots are again very smooth. The development in time of the streamline patterns is displayed in Fig. 20. Noticeable with respect to Fig. 15 is that the the lip vortex is less developed for the FENE model than for the FENE-P constitutive equation. Furthermore, the maximum values of the stream function are much lower. Although it seems that the steady state contains two vortices for the FENE model, this is not exactly the case. Despite the smooth transient stresses, no real steady state value is reached for the streamlines. The maximum stream function is contained in the interval $[5\ 10^{-3}, 1.1\ 10^{-2}]$, and the two vortex situation is alternated with a single corner vortex. The reason for the non-steady behaviour of the low-intensity vortices might be the small stochastic oscillations in the stress. Further mesh refinement and increasing the number of dumbbells N_d per particle should settle the issue.

6 Conclusions

In this paper, we have demonstrated the ability of BLPM to accurately simulate transient flow of viscoelastic fluids, both for macrorheological and microrheological models. The method consists of tracking in each element a small number of Lagrangian particles N steps backward in time. These particles have fixed locations in the reference element; only the particle trajectories change in time. The particle locations can be chosen a priori, so that an almost optimal distribution of particles can be used to evaluate the stress. Furthermore,

highly graded meshes can be handled in a straightforward manner. For obtaining an initial value for the integration along trajectories, an Eulerian configuration data field is stored every time step. N time steps later, the initial value is calculated from this Eulerian field by means of interpolation.

To establish an optimal numerical parameter setting for BLPM, we have considered two benchmark problems: high-eccentricity journal bearing and 4:1 abrupt contraction flow. For the smooth journal bearing flow, the influence of the numerical parameters on the accuracy of the stress transients has been investigated. The key point for the accuracy is the initialisation step. When a spatially second-order accurate Eulerian field is used for initialisation, we have shown that the accuracy is independent of the number of backward steps N. Only a single step of integration backward in time is sufficient to obtain accurate results, even for very small time steps. The stress transients also compare well with results obtained with a conventional mixed finite element approach and the forward-tracking Lagrangian particle method LPM. This applies both to constitutive equations and kinetic theory models. The stability of the method has been demonstrated for the non-smooth 4:1 contraction flow. Smooth transients for the stresses could be obtained, even near and at the sharp corner, both for the macroscopic and microscopic stress models. Furthermore, stress contours showed smoothness in space, except for a small region close to the sharp corner where steep gradients are present.

The benefit of BLPM lies in its efficiency. Accurate results are obtained by tracking backward in time over one single step only. This makes the method attractive to use with kinetic theory models, for which CPU time and memory requirements are very demanding.

7 Acknowledgements

We wish to thank Antony Beris, Xavier Gallez, Pierre Halin and Gregory Lielens for helpful discussion. This work is supported by the ARC 97/02-210 project, Communauté Française de Belgique, and the EC TMR contract FMRX-CT98-0210. The work of V. Legat is supported by the Belgian Fonds National de la Recherche Scientifique (FNRS).

References

[1] M. Laso and H. C. Öttinger. Calculation of viscoelastic flow using molecular models: the CONNFFESSIT approach. *J. Non-Newtonian Fluid Mech.*, 47:1–20, 1993.

[2] M.A. Hulsen, A.P.G. van Heel, and B.H.A.A. van den Brule. Simulation of viscoelastic flows using Brownian configuration fields. *J. Non-Newtonian Fluid Mech.*, 70:79–101, 1997.

[3] P. Halin, G. Lielens, R. Keunings, and V. Legat. The Lagrangian particle method for macroscopic and micro-macro viscoelastic flow computations. *J. Non-Newtonian Fluid Mech.*, 79:387–403, 1998.

[4] R.B. Bird, C.F. Curtiss, R.C. Armstrong, and O. Hassager. *Dynamics of Polymer Liquids*, volume 2. John Wiley, New York, 2nd edition, 1987.

[5] H. C. Öttinger. *Stochastic Processes in Polymeric Fluids*. Springer Verlag, Berlin, 1996.

[6] R. Guénette and M. Fortin. A new mixed finite element method for computing viscoelastic flows. *J. Non-Newtonian Fluid Mech.*, 60:27–52, 1995.

[7] F.P.T. Baaijens. An iterative solver for the DEVSS/DG method with application to smooth and non-smooth flows of upper convected Maxwell fluid. *J. Non-Newtonian Fluid Mech.*, 75:119–138, 1998.

[8] X. Gallez, P. Halin, G. Lielens, R. Keunings, and V. Legat. The adaptive Lagrangian particle method for microscopic and micro-macro computations of time-dependent viscoelastic flows. *Comp. Meth. Appl. Mech. Eng.*, 1999. In press.

[9] A. Goublomme, B. Draily, and M.J. Crochet. Numerical prediction of extrudate swell of a high-density polyethylene. *J. Non-Newtonian Fluid Mech.*, 44:171–195, 1992.

[10] R. Keunings. On the Peterlin approximation for finitely extensible dumbbells. *J. Non-Newtonian Fluid Mech.*, 68:85–100, 1997.

[11] A.C. Öttinger, B.H.A.A. van den Brule, and M.A. Hulsen. Brownian configuration fields and variance reduced CONNFFESSIT. *J. Non-Newtonian Fluid Mech.*, 70:255–261, 1997.

[12] B. Purnode and M.J. Crochet. Flows of polymer solutions through contractions. Part 1: flows of polyacrylamide solutions through planar contractions. *J. Non-Newtonian Fluid Mech.*, 65:269–289, 1996.

Figure legend

Figure 1: Particle path in finite element mesh for the case $N = 3$; a $\bullet$ denotes the fixed location where the stress has to be calculated, a $\bullet$ the intermediate positions on the particle path leading to it.

Figure 2: One-dimensional illustration of violation of constraints due to least-squares fit, extrapolation and non-linear polynomial interpolation; thick lines indicate parts of the curves in the non-physical shaded regions.

Figure 3: Two examples of distributions of particle positions over an element: 9 ppe (nodal points) and 13 ppe.

Figure 4: Coarse mesh (10x40 elements) for journal bearing flow with indicated in zoom where stress values are displayed in subsequent figures.

Figure 5: Transients of stress for various values of N for FENE-P model using BLPM; mesh 10x40, $\Delta t = 10^{-2}$, DEVSS, linear $\boldsymbol{F}^{\mathrm{E}}$, 9 ppe.

Figure 6: Transients of stress for various values of N for FENE-P model using BLPM; mesh 10x40, $\Delta t = 10^{-2}$, DEVSS, quadratic $\boldsymbol{F}^{\mathrm{E}}$, 9 ppe.

Figure 7: Transients of stress for various values of N for FENE-P model using BLPM; mesh 20x80, $\Delta t = 10^{-2}$, DEVSS, quadratic $\boldsymbol{F}^{\mathrm{E}}$, 9 ppe.

Figure 8: Behaviour with mesh refinement of transient of stresses for FENE-P using BLPM; $\Delta t = 10^{-2}$, DEVSS, $N = 1$, quadratic $\boldsymbol{F}^{\mathrm{E}}$, 9 ppe.

Figure 9: Transients of stress for various values of Δt for FENE-P using BLPM; mesh 10x40, DEVSS, $N = 1$, quadratic $\boldsymbol{F}^{\mathrm{E}}$, 9 ppe.

Figure 10: Transients of stress for various values of Δt including and excluding DEVSS, for FENE-P using BLPM; mesh 20x80, $N = 1$, quadratic $\boldsymbol{F}^{\mathrm{E}}$, 9 ppe.

Figure 11: Comparison of transients of stress for FENE-P using BLPM, with LPM and a conventional mixed finite element method; mesh 10x40, $\Delta t = 10^{-2}$. BLPM: DEVSS, $N = 1$, quadratic $\boldsymbol{F}^{\mathrm{E}}$, 9 ppe. LPM: on average 1600 ppe.

Figure 12: Comparison of transients of stress for FENE-P using BLPM, with LPM; mesh 20x80, $\Delta t = 10^{-2}$. BLPM: DEVSS, $N = 1$, quadratic $\boldsymbol{F}^{\mathrm{E}}$, 9 ppe. LPM: on average 1600 ppe.

Figure 13: Transients of stress for FENE model using BLPM and ALPM, and FENE-P curve for reference; mesh 10x40, $\Delta t = 10^{-2}$. BLPM: DEVSS, $N = 1$, quadratic $\boldsymbol{F}^{\mathrm{E}}$, 9 ppe. ALPM: between 9 and 20 ppe.

Figure 14: Coarse mesh (465 elements) near sharp corner for 4:1 contraction flow with indicated in zoom where stress values are displayed in subsequent figures.

Figure 15: Development in time of streamlines and maximum value of stream function Ψ in recirculation zone for FENE-P model using BLPM; fine mesh, $\Delta t = 10^{-3}$, DEVSS/CG, $N = 1$, 9 ppe.

Figure 16: Contour lines of stress in steady state near sharp corner for FENE-P model using BLPM; fine mesh, $\Delta t = 10^{-3}$, DEVSS/CG, $N = 1$, 9 ppe. Plotted contour lines: 0, 1, 2, 3, 4, 5, and all tens. a) τ_{xx}: 15 contours between -0.62 and 92, b) τ_{xy}: 8 contours between -0.60 and 22, c) τ_{yy}: 7 contours between -0.88 and 14.

Figure 17: Transients of stress at corner (Fig. 14) for FENE-P using BLPM with various particle locations and meshes; $N = 1$, DEVSS/CG, $\Delta t = 10^{-3}$.

Figure 18: Transients of stress at and near corner (Fig. 14) for FENE model using BLPM; coarse mesh, $\Delta t = 10^{-3}$, DEVSS, $N = 1$, 9 ppe.

Figure 19: Contour lines of stress in steady state near sharp corner for FENE model using BLPM; coarse mesh, $\Delta t = 10^{-3}$, DEVSS, $N = 1$, 9 ppe. Plotted contour lines: 0, 1, 2, 3, 4, 5, and all tens. a) τ_{xx}: 12 contours between -3.0 and 70, b) τ_{xy}: 10 contours between -3.4 and 41, c) τ_{yy}: 10 contours between -3.3 and 40.

Figure 20: Development in time of streamlines and maximum value of stream function Ψ in recirculation zone for FENE model using BLPM; coarse mesh, $\Delta t = 10^{-3}$, DEVSS, $N = 1$, 9 ppe.

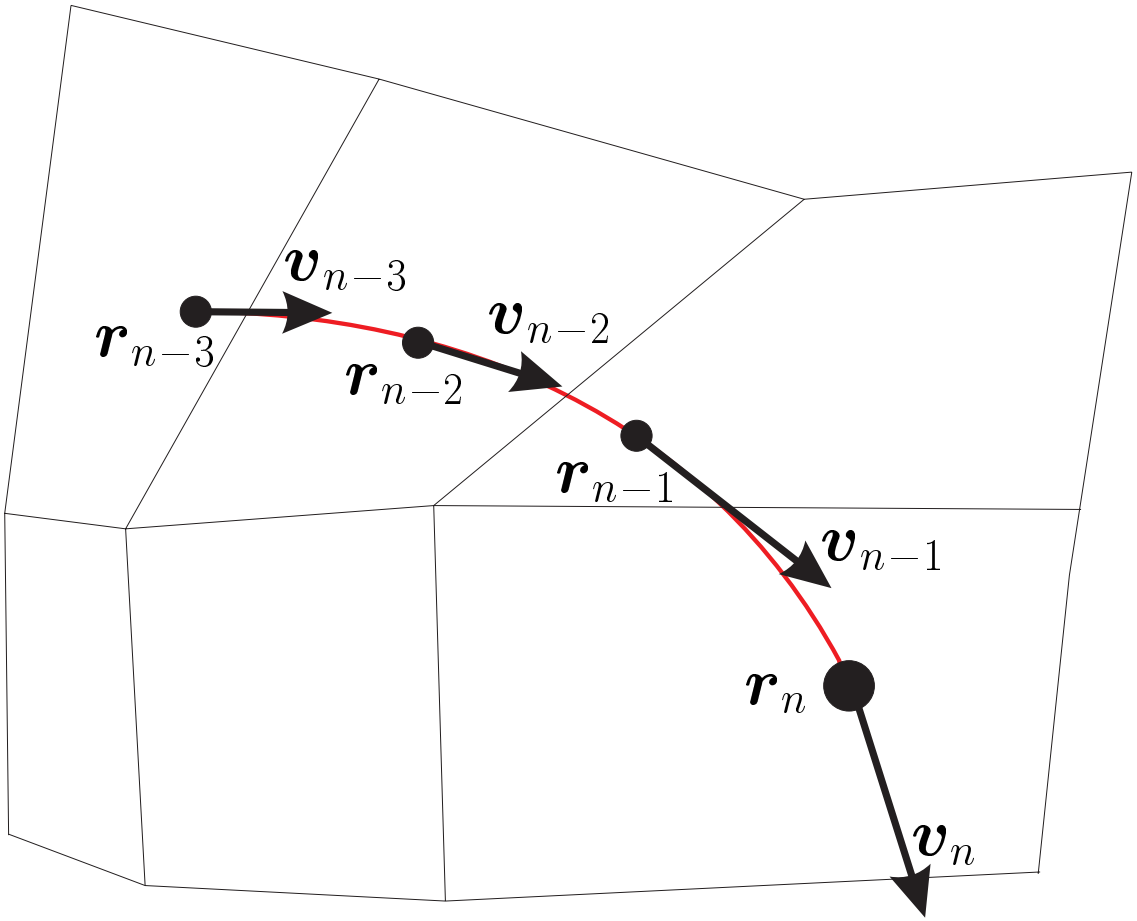

Figure 1: Particle path in finite element mesh for the case $N = 3$; a ● denotes the fixed location where the stress has to be calculated, a • the intermediate positions on the particle path leading to it.

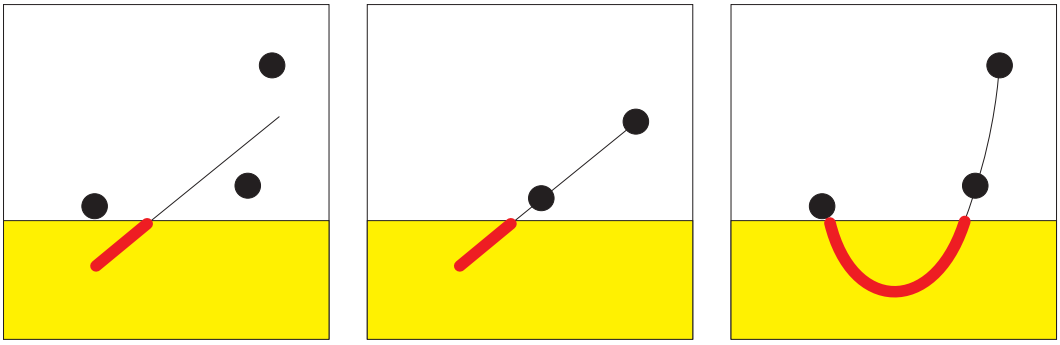

Figure 2: One-dimensional illustration of violation of constraints due to least-squares fit, extrapolation and non-linear polynomial interpolation; thick lines indicate parts of the curves in the non-physical shaded regions.

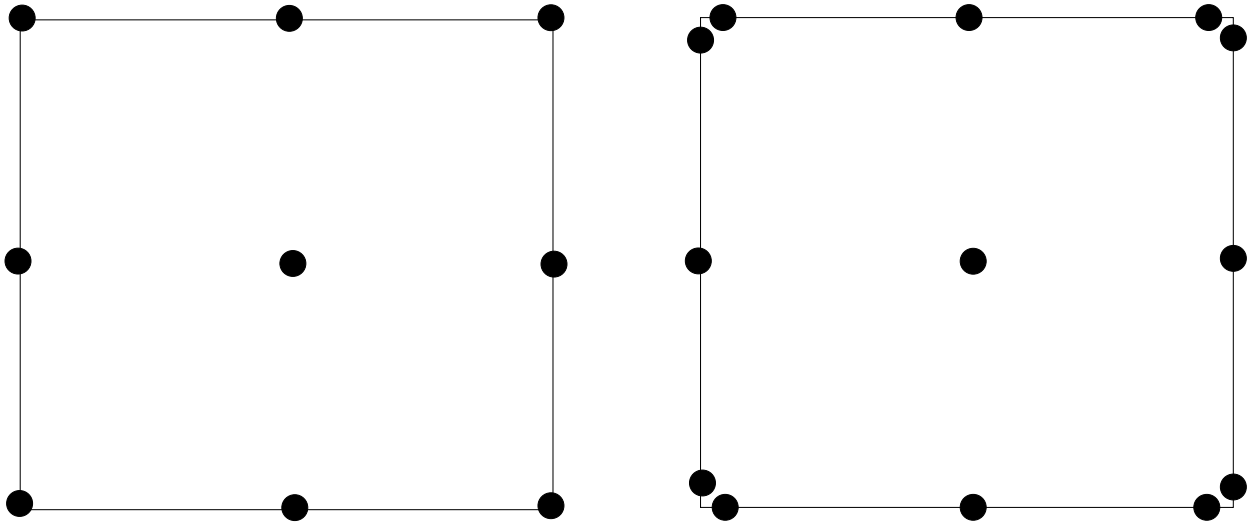

Figure 3: Two examples of distributions of particle positions over an element: 9 ppe (nodal points) and 13 ppe.

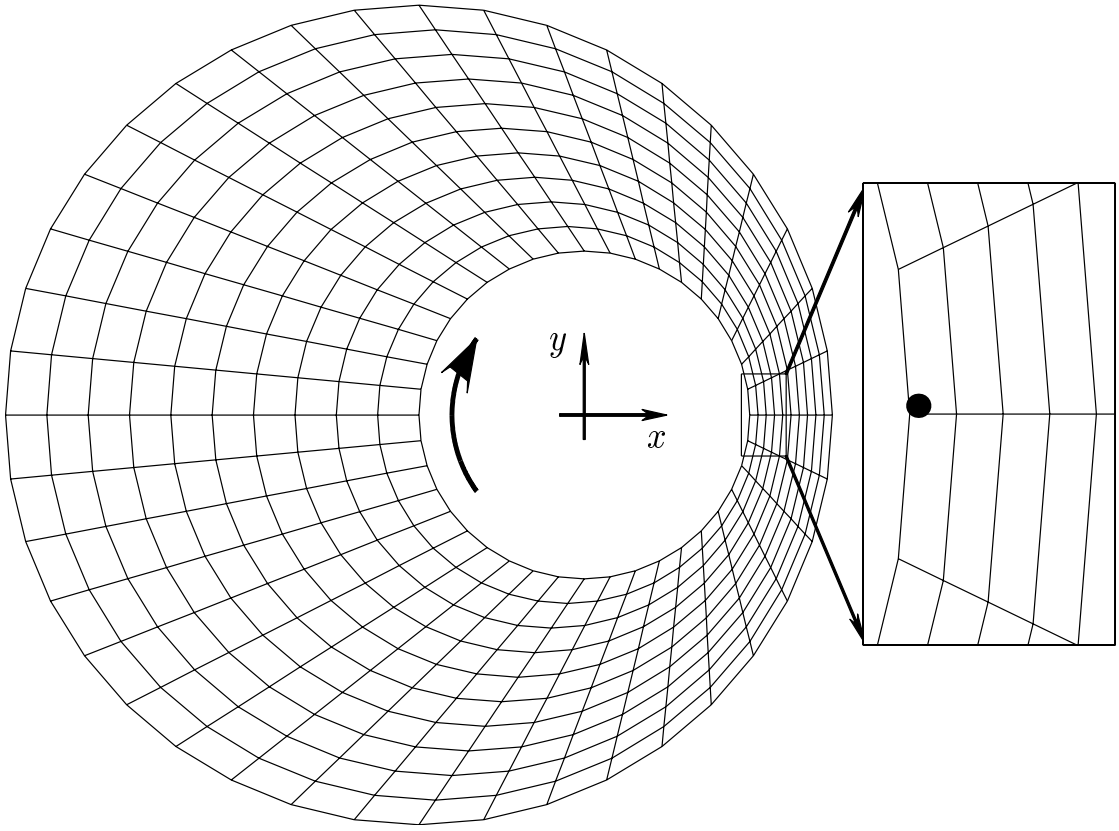

Figure 4: Coarse mesh (10x40 elements) for journal bearing flow with indicated in zoom where stress values are displayed in subsequent figures.

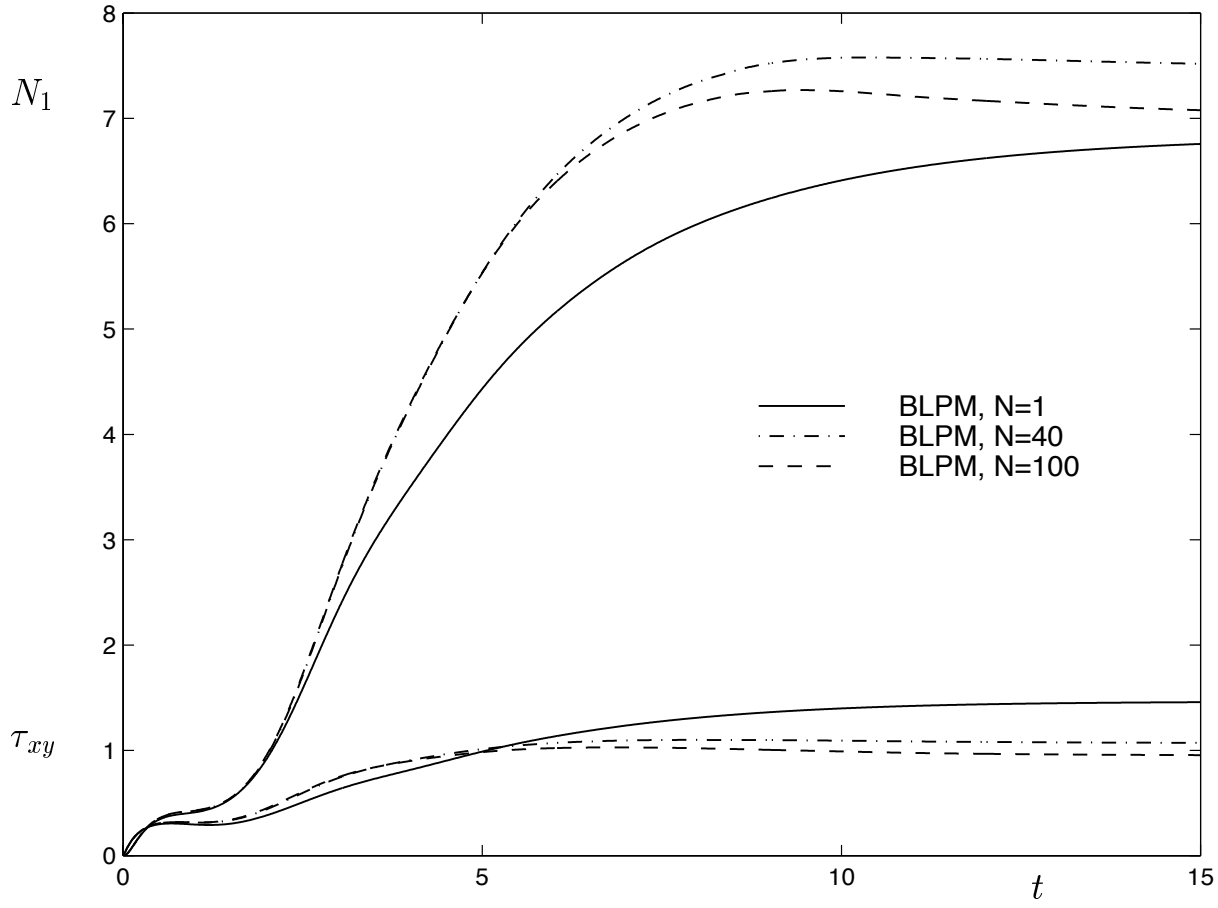

Figure 5: Transients of stress for various values of N for FENE-P model using BLPM; mesh 10x40, $\Delta t = 10^{-2}$, DEVSS, linear $\boldsymbol{F}^{\mathrm{E}}$, 9 ppe.

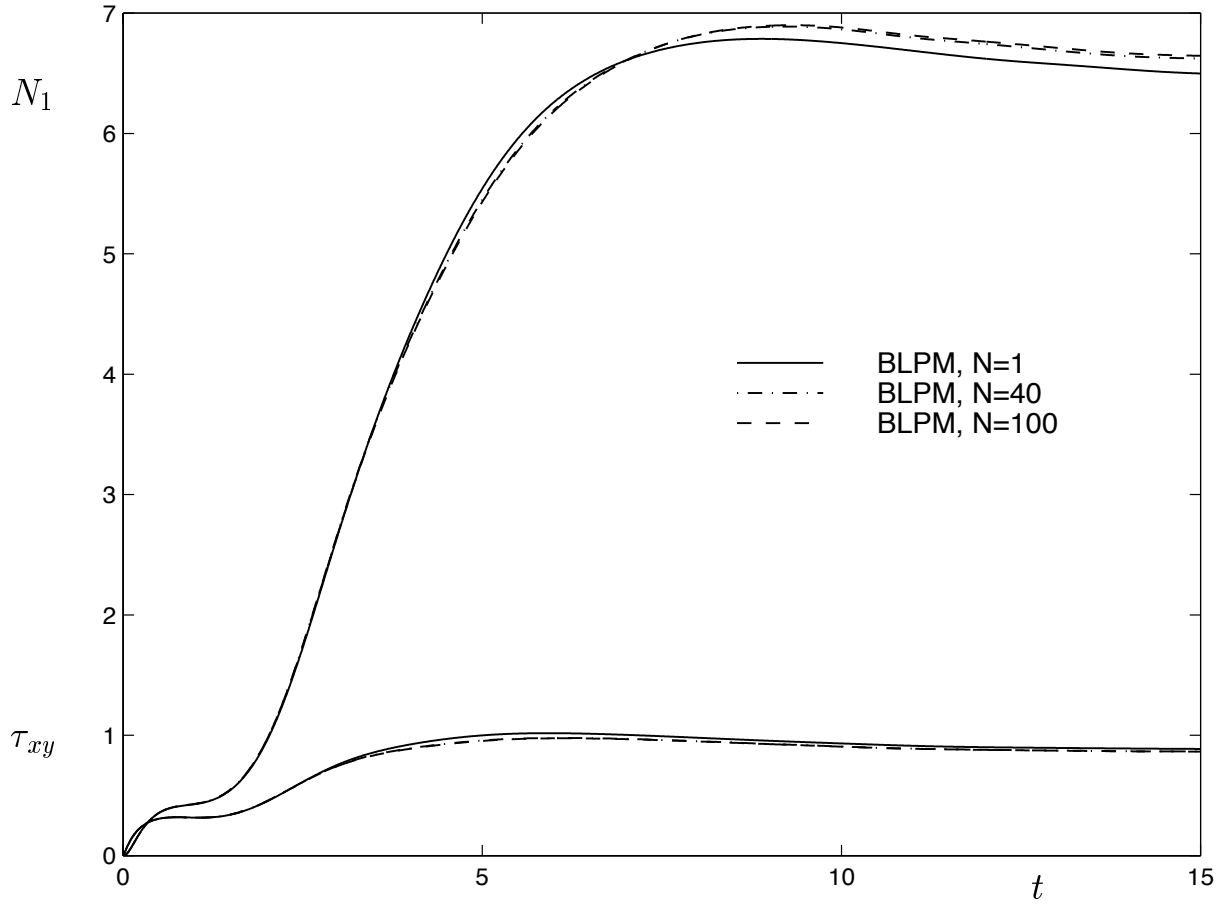

Figure 6: Transients of stress for various values of N for FENE-P model using BLPM; mesh 10x40, $\Delta t = 10^{-2}$, DEVSS, quadratic $\boldsymbol{F}^{\mathrm{E}}$, 9 ppe.

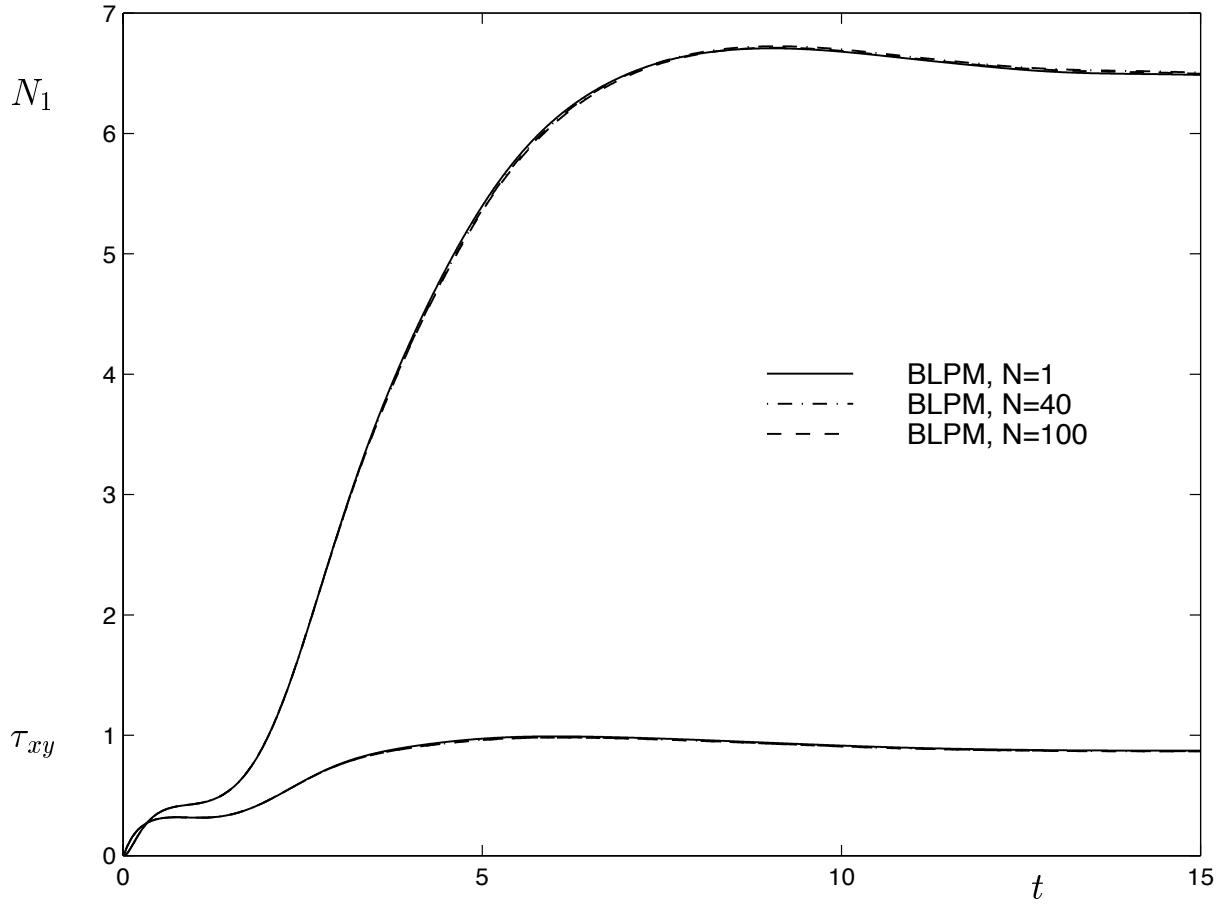

Figure 7: Transients of stress for various values of N for FENE-P model using BLPM; mesh 20x80, $\Delta t = 10^{-2}$, DEVSS, quadratic $\boldsymbol{F}^{\mathrm{E}}$, 9 ppe.

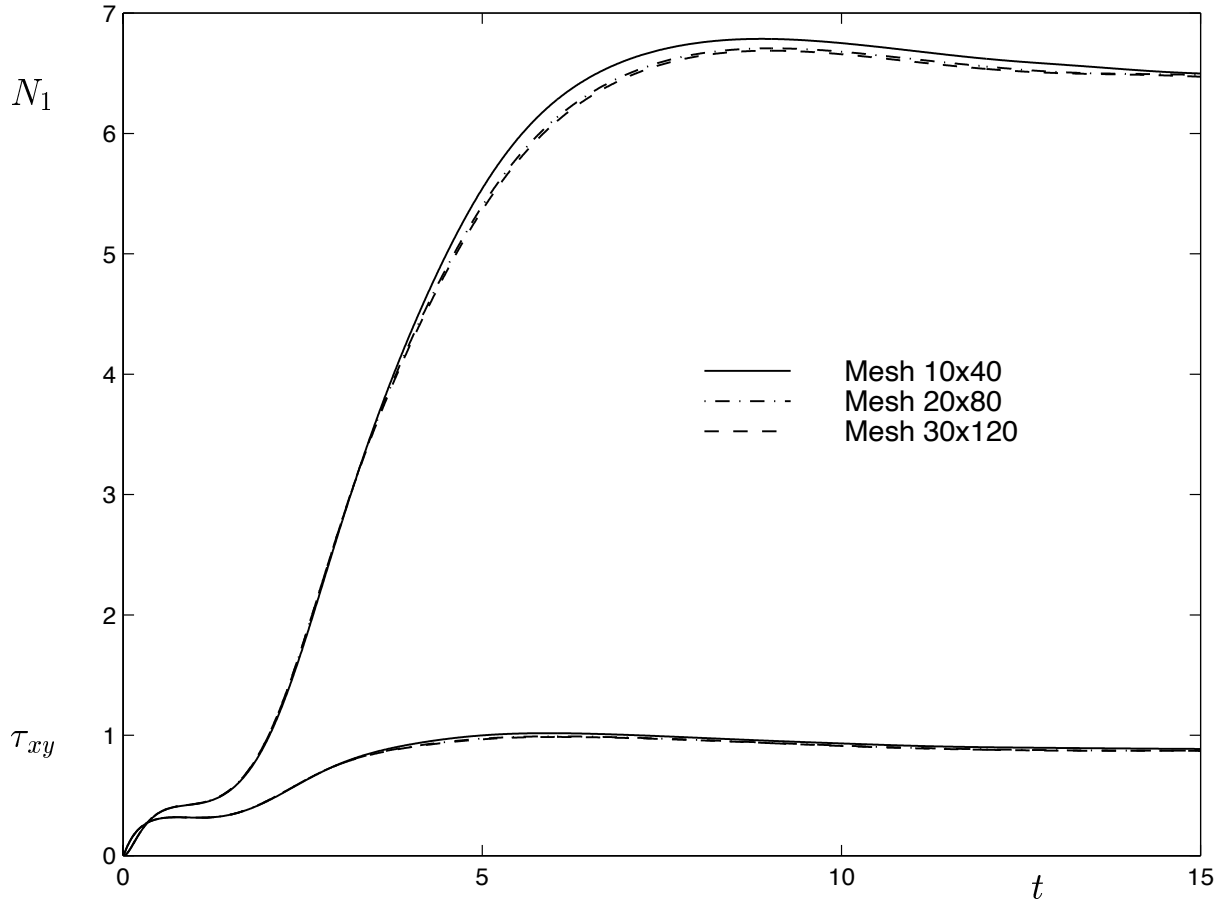

Figure 8: Behaviour with mesh refinement of transient of stresses for FENE-P using BLPM; $\Delta t = 10^{-2}$, DEVSS, $N = 1$, quadratic $\boldsymbol{F}^{\mathrm{E}}$, 9 ppe.

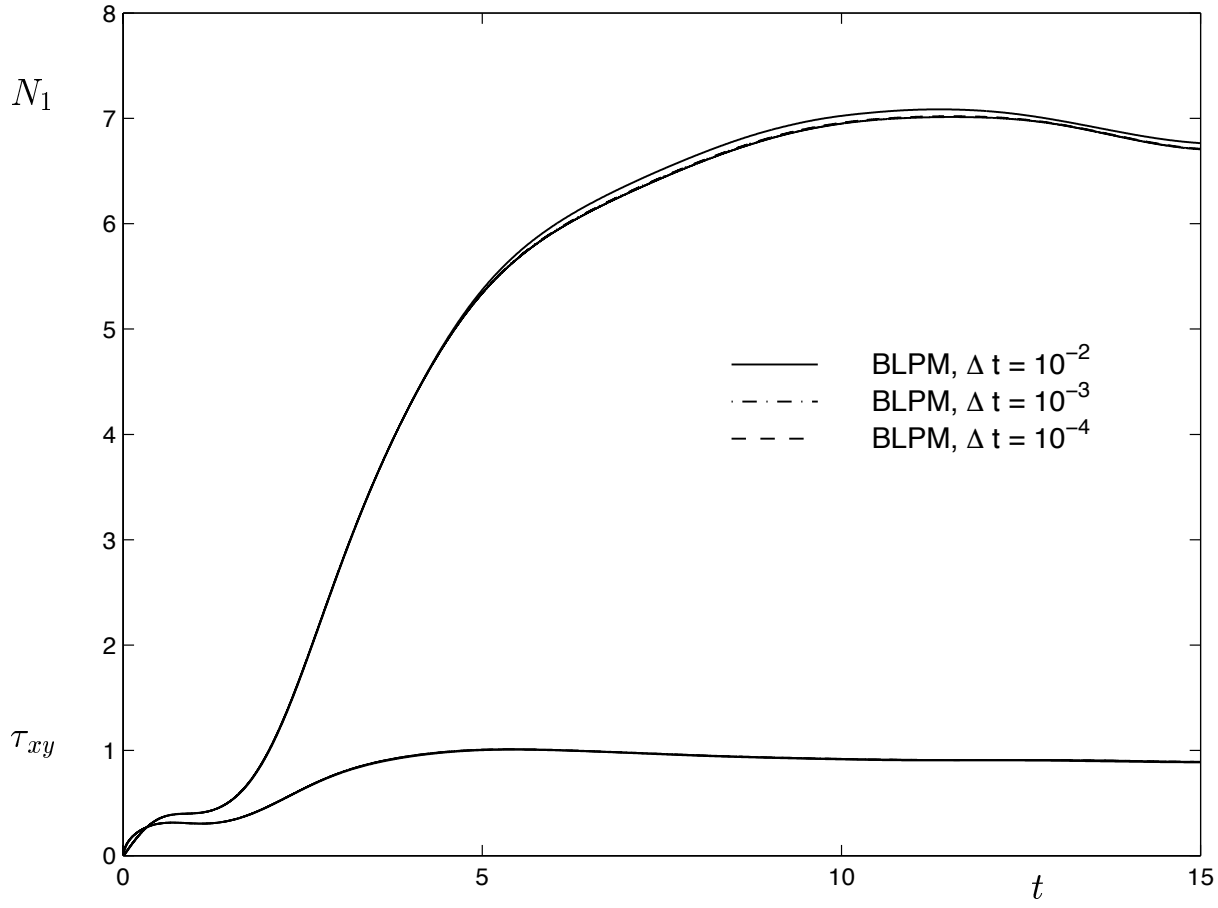

Figure 9: Transients of stress for various values of Δt for FENE-P using BLPM; mesh 10x40, DEVSS, $N = 1$, quadratic $\boldsymbol{F}^{\mathrm{E}}$, 9 ppe.

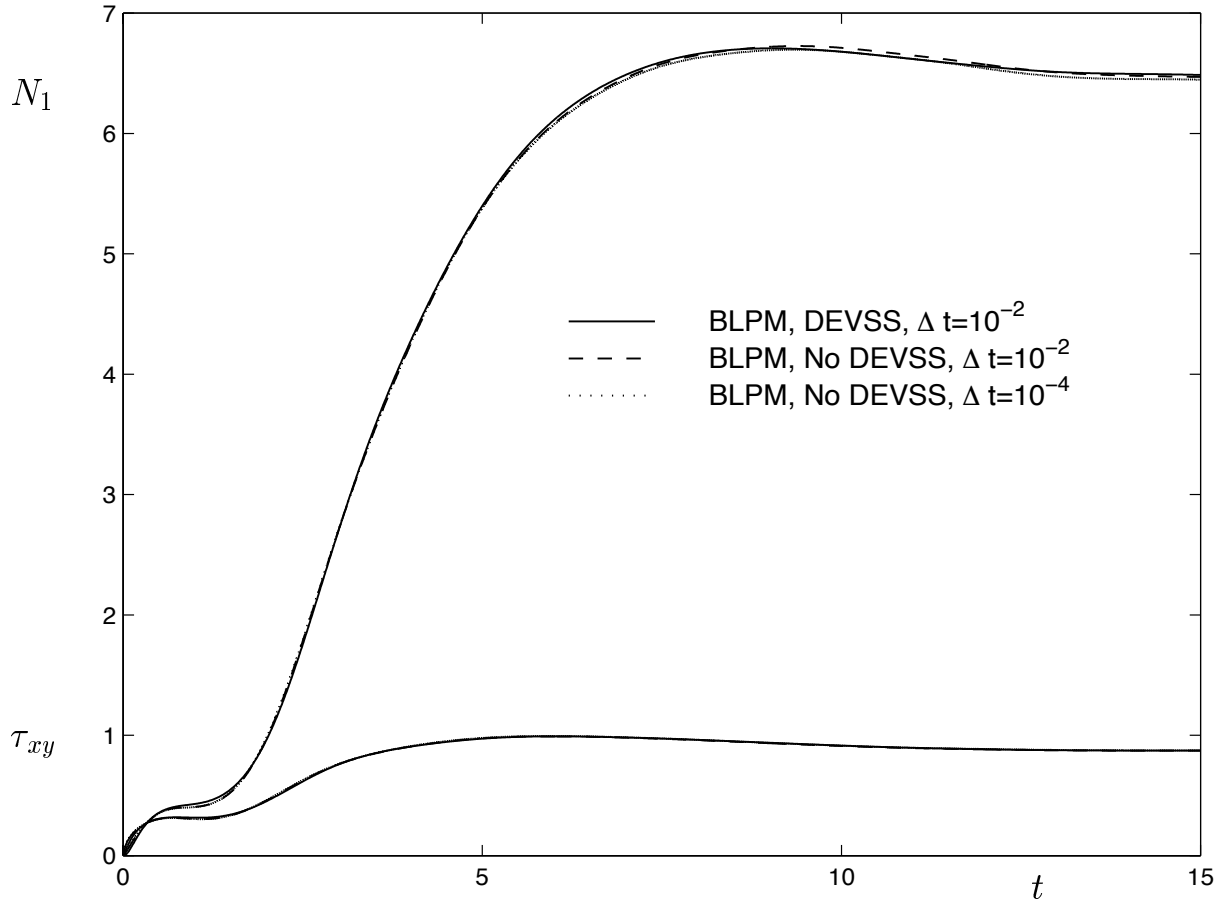

Figure 10: Transients of stress for various values of Δt including and excluding DEVSS, for FENE-P using BLPM; mesh 20x80, $N = 1$, quadratic $\boldsymbol{F}^{\mathrm{E}}$, 9 ppe.

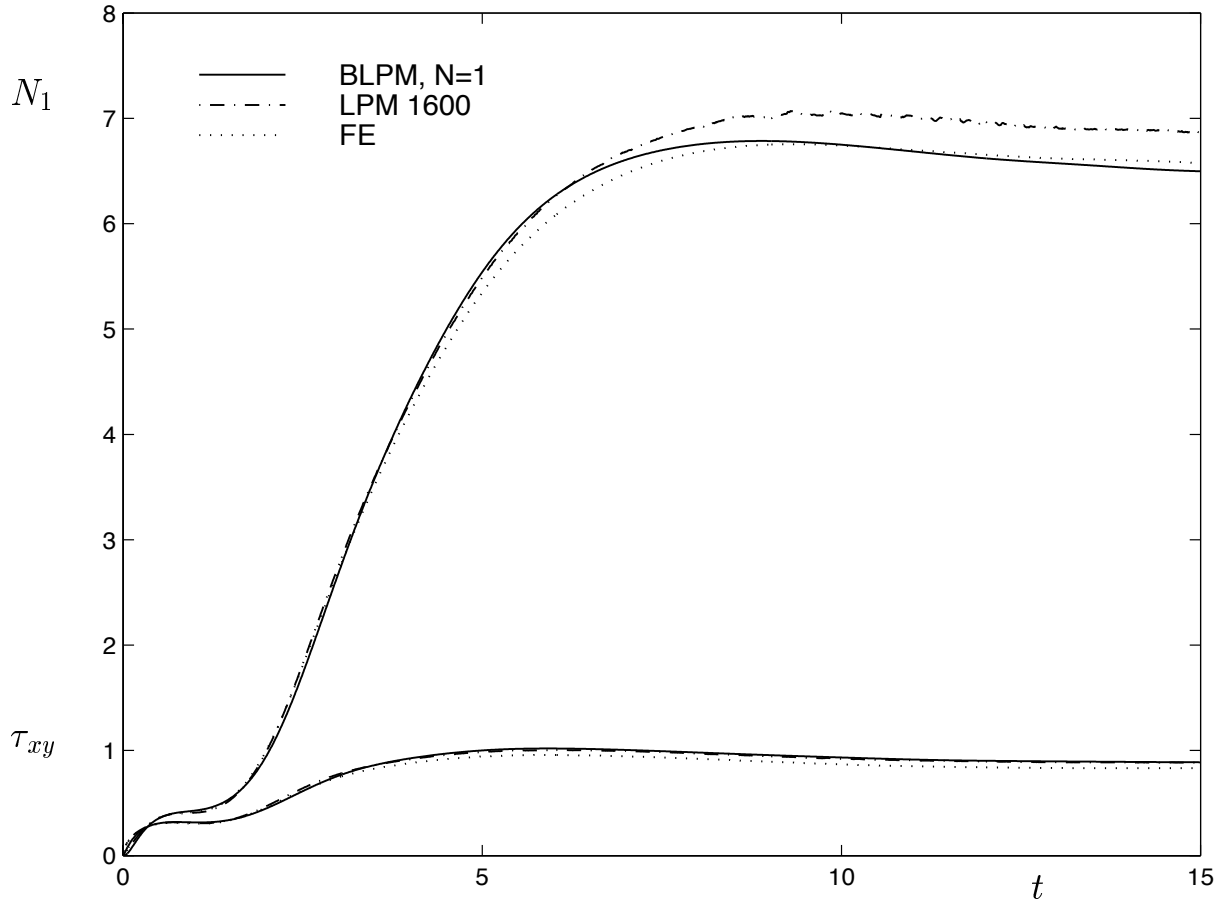

Figure 11: Comparison of transients of stress for FENE-P using BLPM, with LPM and a conventional mixed finite element method; mesh 10x40, $\Delta t = 10^{-2}$. BLPM: DEVSS, $N = 1$, quadratic $\boldsymbol{F}^{\mathrm{E}}$, 9 ppe. LPM: on average 1600 ppe.

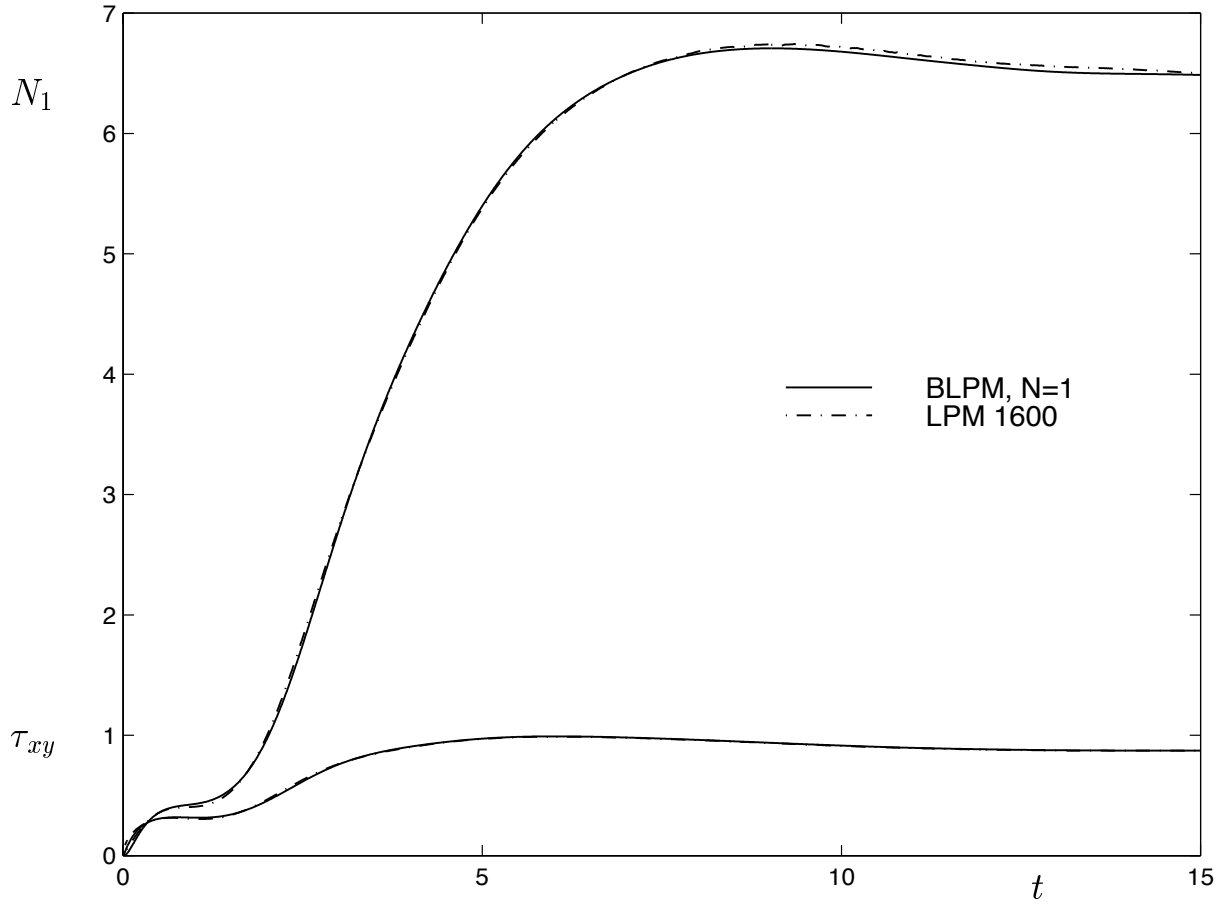

Figure 12: Comparison of transients of stress for FENE-P using BLPM, with LPM; mesh 20x80, $\Delta t = 10^{-2}$. BLPM: DEVSS, $N = 1$, quadratic $\boldsymbol{F}^{\mathrm{E}}$, 9 ppe. LPM: on average 1600 ppe.

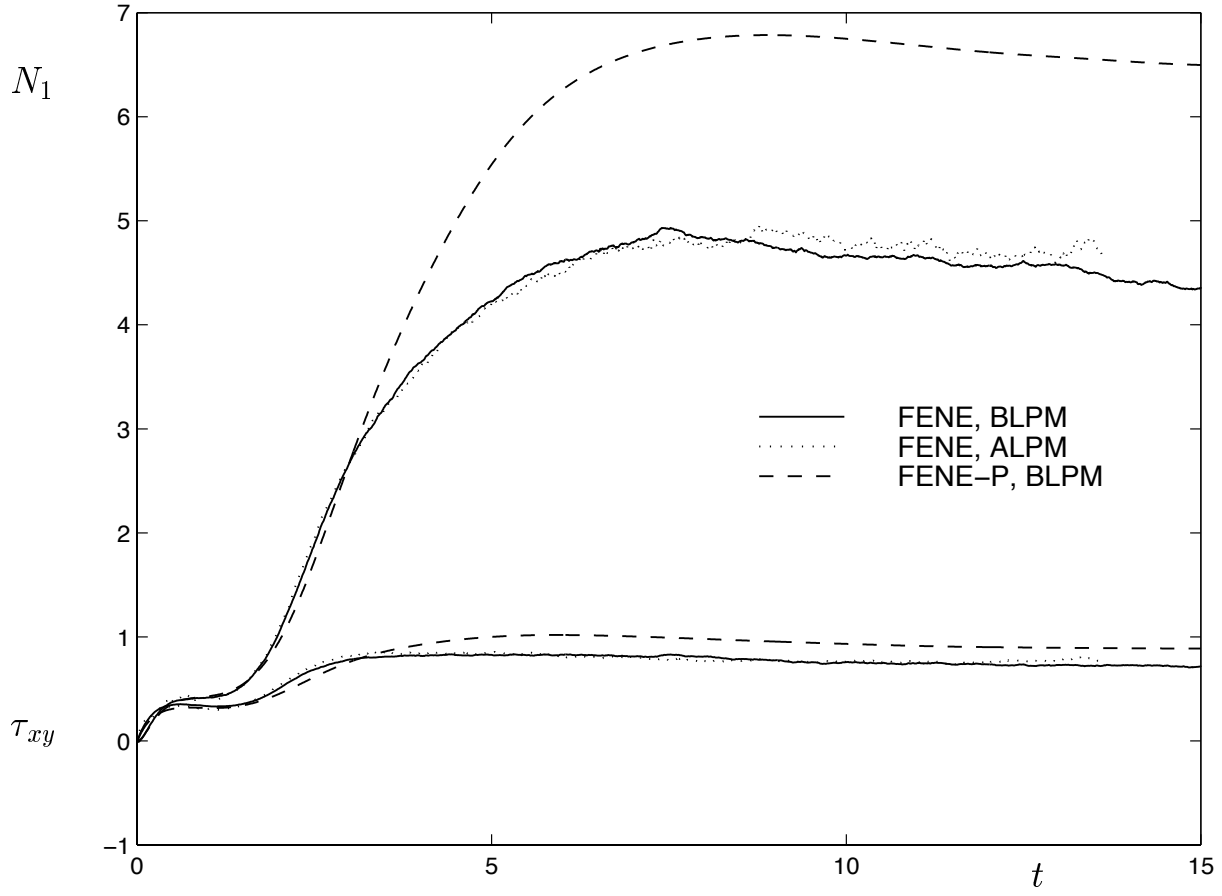

Figure 13: Transients of stress for FENE model using BLPM and ALPM, and FENE-P curve for reference; mesh 10x40, $\Delta t = 10^{-2}$. BLPM: DEVSS, $N = 1$, quadratic $\boldsymbol{F}^{\mathrm{E}}$, 9 ppe. ALPM: between 9 and 20 ppe.

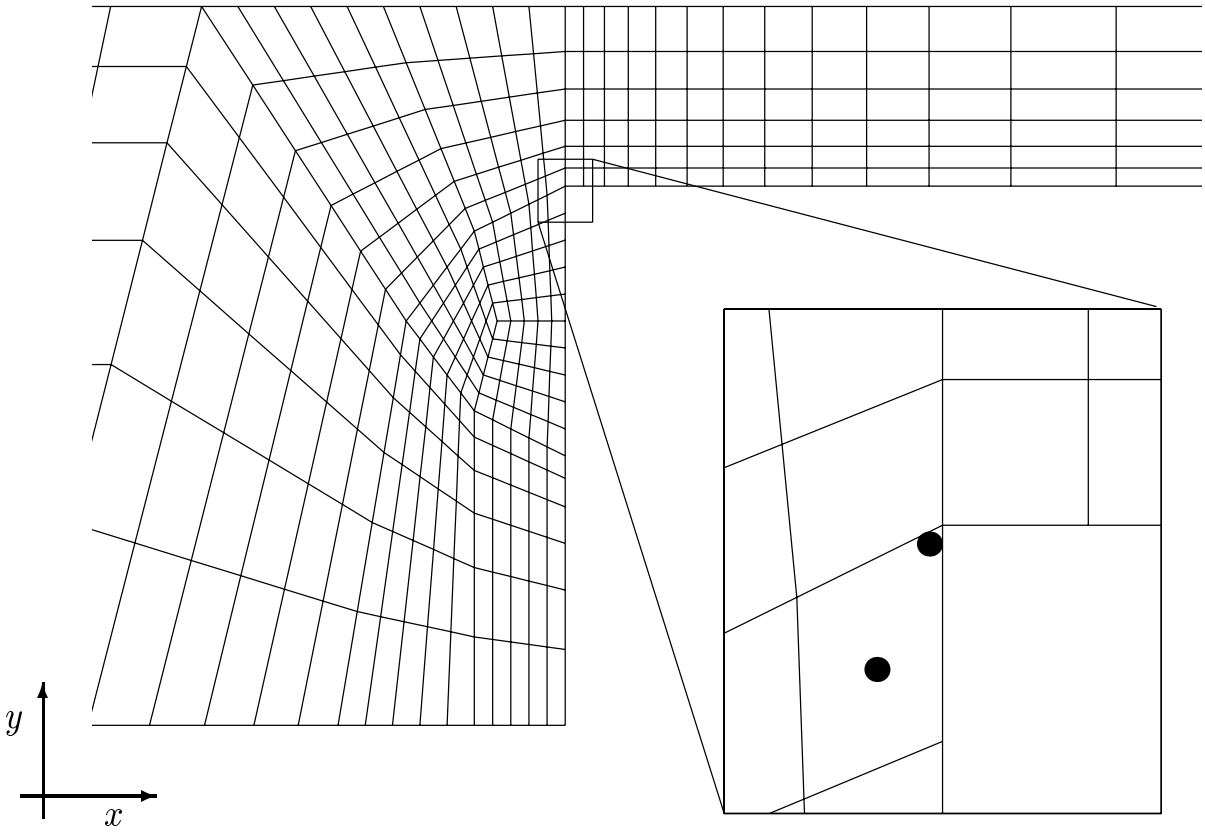

Figure 14: Coarse mesh (465 elements) near sharp corner for 4:1 contraction flow with indicated in zoom where stress values are displayed in subsequent figures.

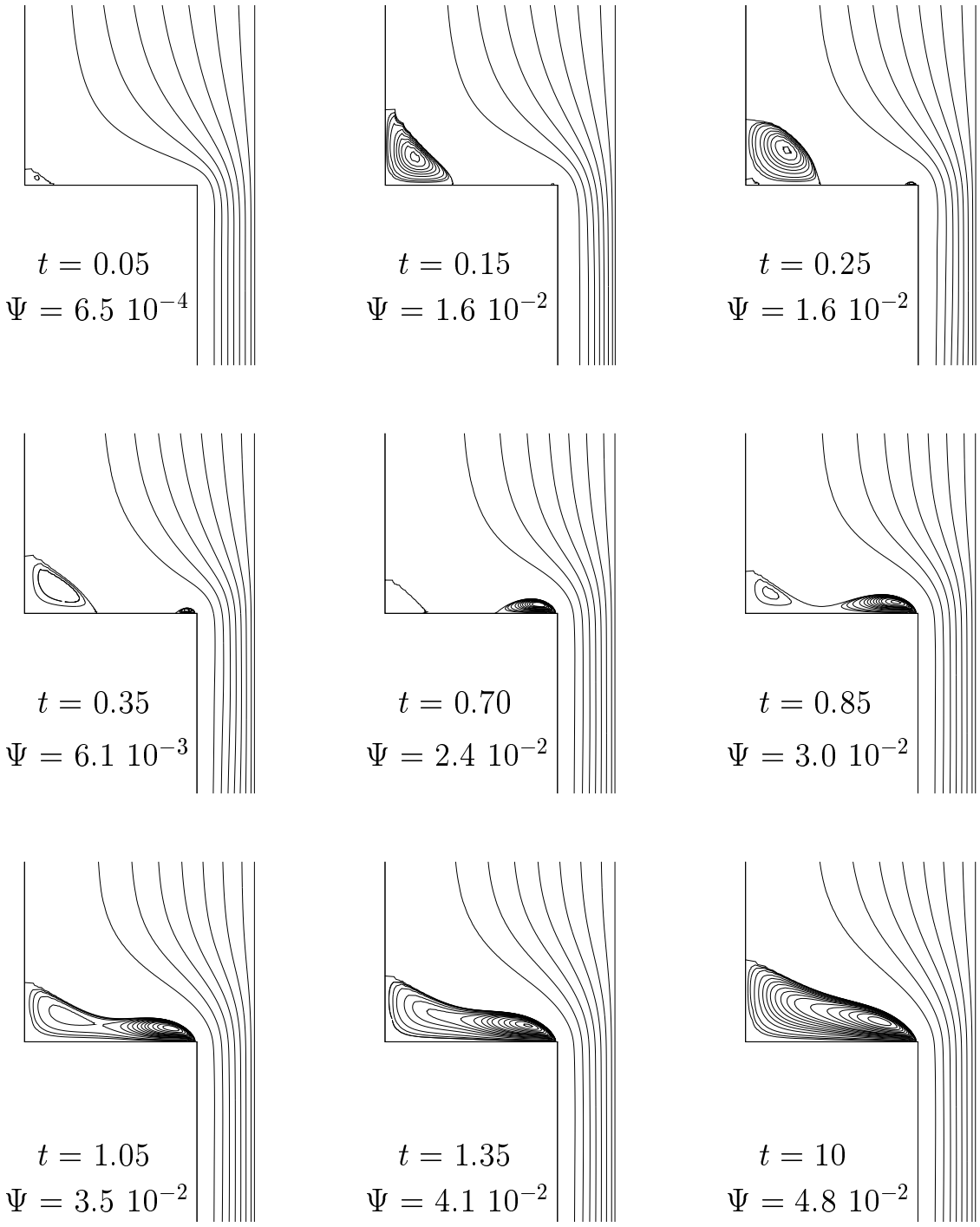

Figure 15: Development in time of streamlines and maximum value of stream function Ψ in recirculation zone for FENE-P model using BLPM; fine mesh, $\Delta t = 10^{-3}$, DEVSS/CG, $N = 1$, 9 ppe.

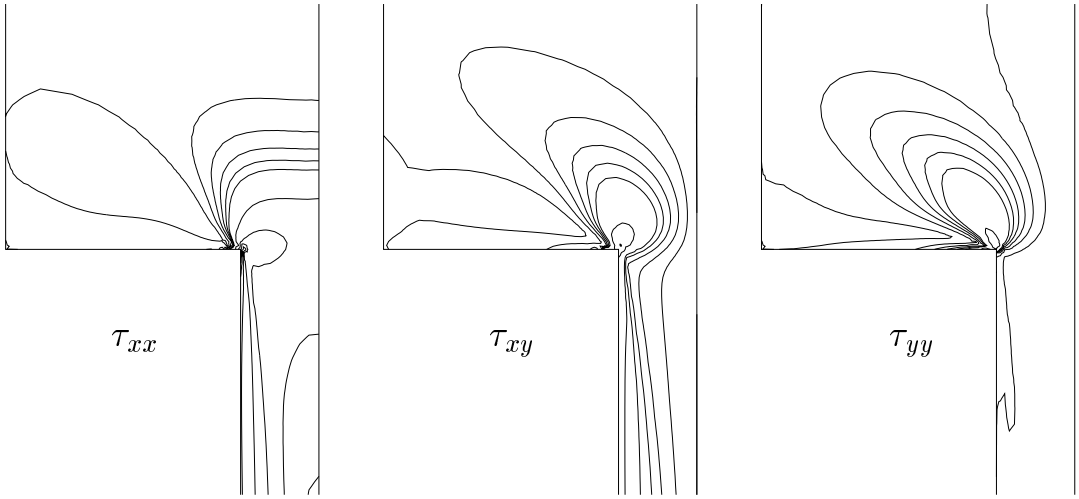

Figure 16: Contour lines of stress in steady state near sharp corner for FENE-P model using BLPM; fine mesh, $\Delta t = 10^{-3}$, DEVSS/CG, $N = 1$, 9 ppe. Plotted contour lines: 0, 1, 2, 3, 4, 5, and all tens. a) τ_{xx}: 15 contours between -0.62 and 92, b) τ_{xy}: 8 contours between -0.60 and 22, c) τ_{yy}: 7 contours between -0.88 and 14.

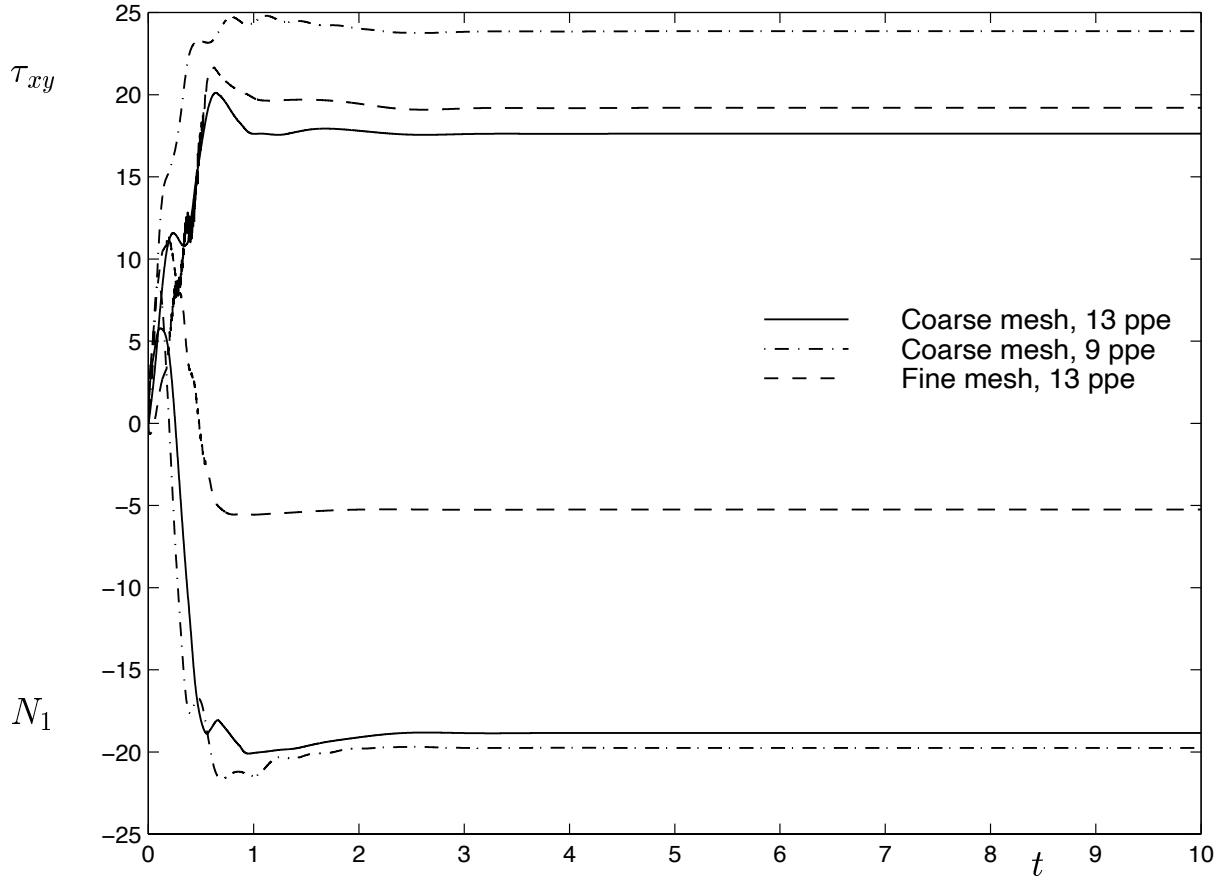

Figure 17: Transients of stress at corner (Fig. 14) for FENE-P using BLPM with various particle locations and meshes; $N = 1$, DEVSS/CG, $\Delta t = 10^{-3}$.

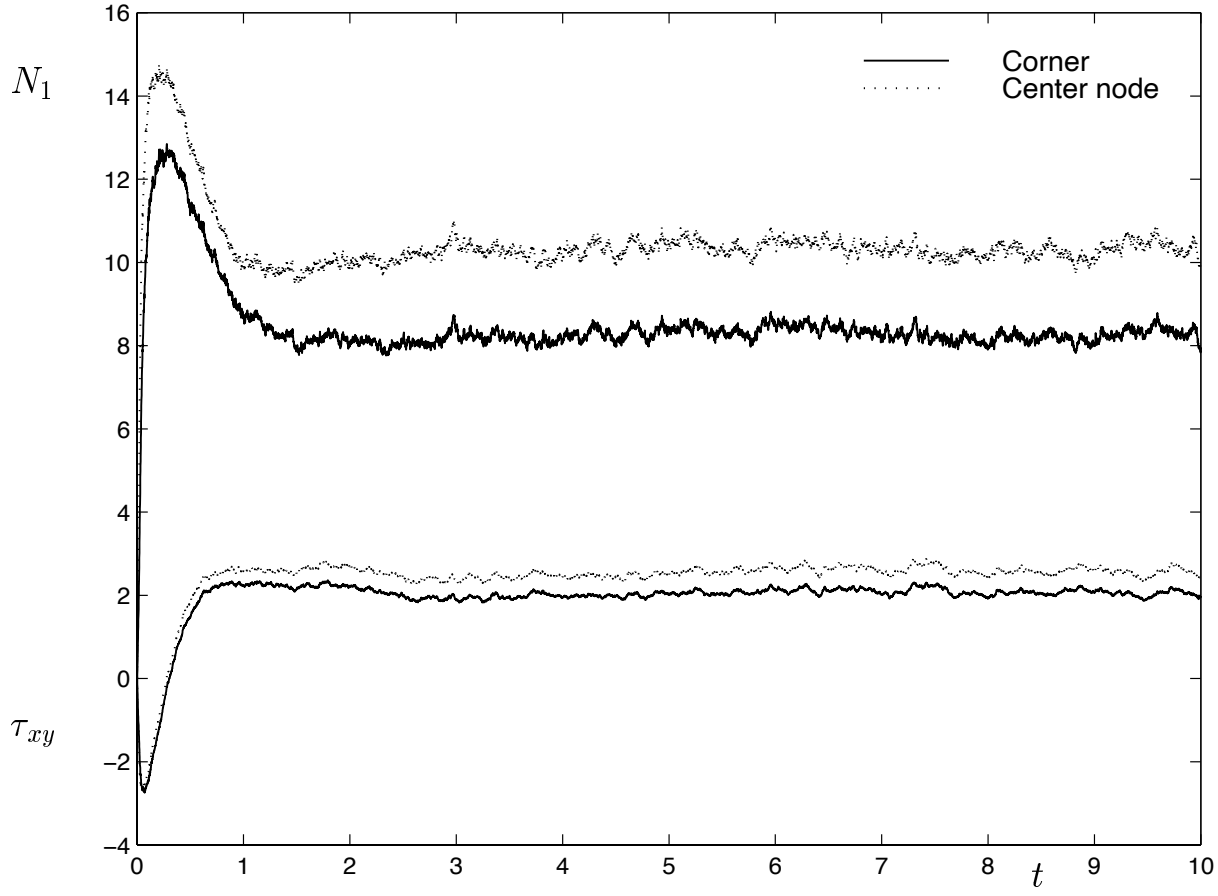

Figure 18: Transients of stress at and near corner (Fig. 14) for FENE model using BLPM; coarse mesh, $\Delta t = 10^{-3}$, DEVSS, $N = 1$, 9 ppe.

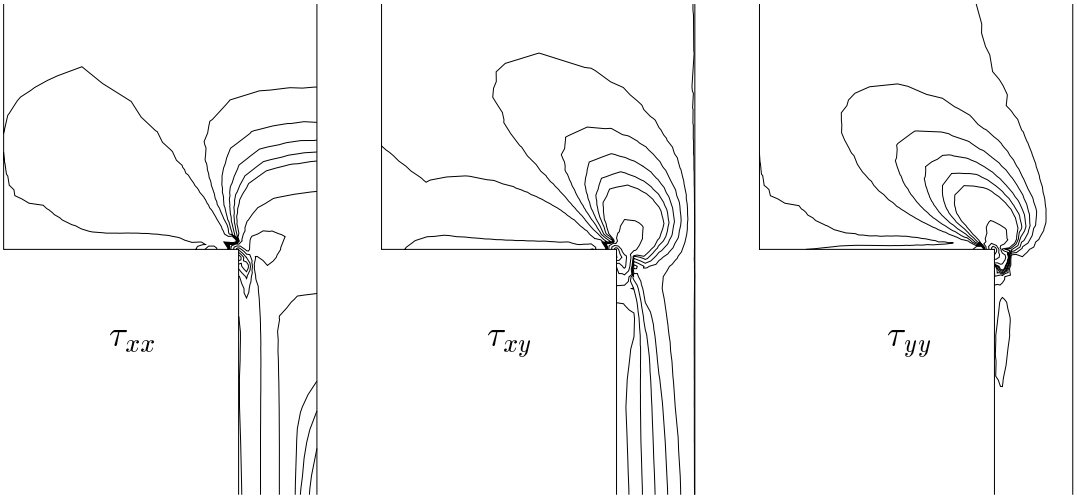

Figure 19: Contour lines of stress in steady state near sharp corner for FENE model using BLPM; coarse mesh, $\Delta t = 10^{-3}$, DEVSS, $N = 1$, 9 ppe. Plotted contour lines: 0, 1, 2, 3, 4, 5, and all tens. a) τ_{xx}: 12 contours between -3.0 and 70, b) τ_{xy}: 10 contours between -3.4 and 41, c) τ_{yy}: 10 contours between -3.3 and 40.

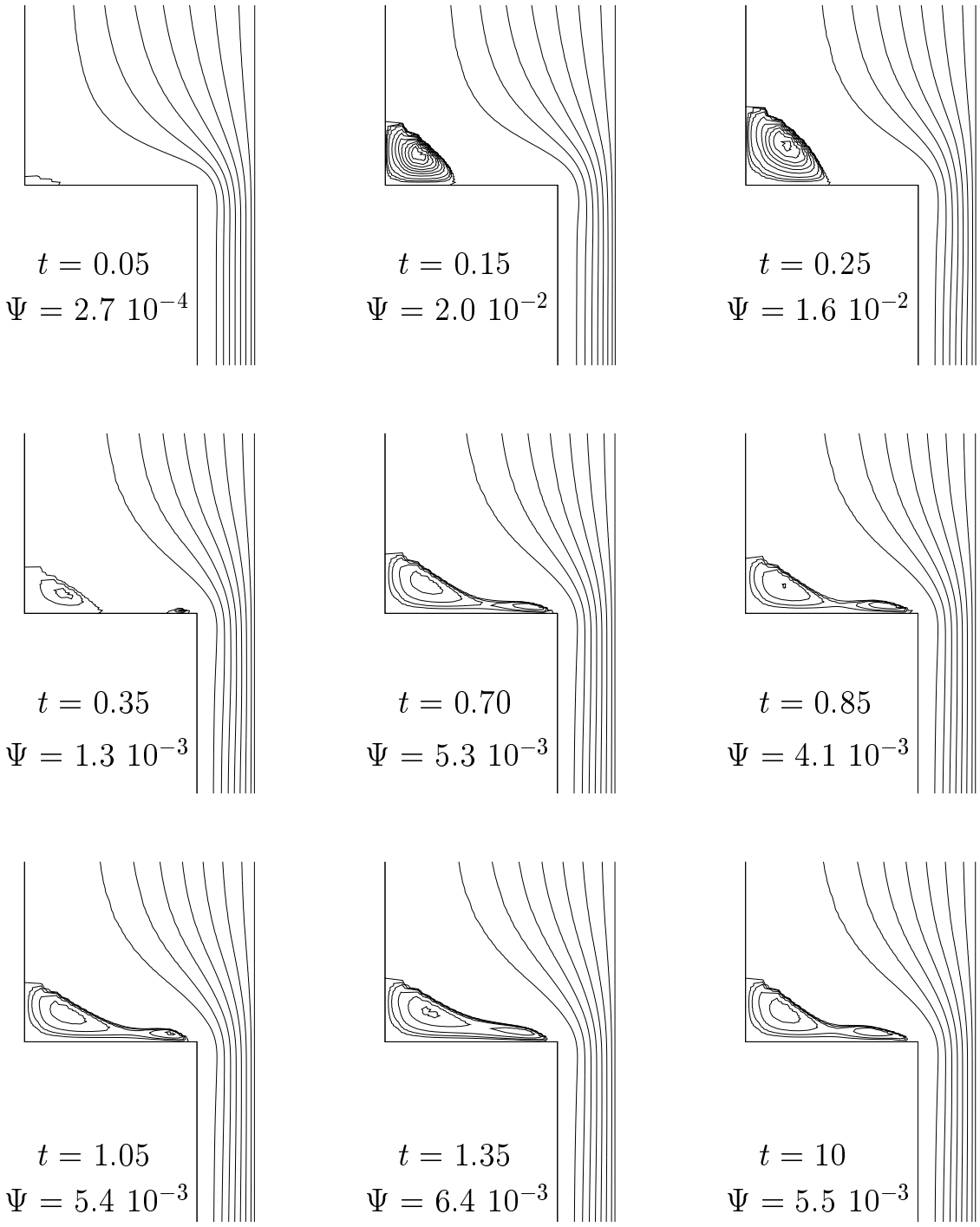

Figure 20: Development in time of streamlines and maximum value of stream function Ψ in recirculation zone for FENE model using BLPM; coarse mesh, $\Delta t = 10^{-3}$, DEVSS, $N = 1$, 9 ppe.